INTERNATIONAL JOURNAL FOR NUMERICAL METHODS IN FLUIDS
Int. J. Numer. Meth. Fluids 2001; **36**: 539–595 (DOI: 10.1002/fld.145)

Viscoelastic simulations of stick-slip and die-swell flows

V. Ngamaramvaranggul and M. F. Webster*

Institute of Non-Newtonian Fluid Mechanics, Department of Computer Science, University of Wales, Swansea, U.K.

SUMMARY

Numerical solutions of viscoelastic flows are demonstrated for a time marching, semi-implicit Taylor–Galerkin/pressure-correction algorithm. Steady solutions are sought for free boundary problems involving combinations of die-swell and stick-slip conditions. Flows with and without drag flow are investigated comparatively, so that the influence of the additional component of the drag flow may be analysed effectively. The influence of die-swell is considered that has application to various industrial processes, such as wire coating. Solutions for two-dimensional axisymmetric flows with an Oldroyd-B model are presented that compare favourably with the literature. The study advances our prior fixed domain formulation with this algorithm, into the realm of free-surface viscoelastic flows. The work involves streamline-upwind/Petrov–Galerkin weighting and velocity gradient recovery techniques that are applied upon the constitutive equation. Free surface solution reprojection and a new pressure-drop/mass balance scheme are proposed. Copyright © 2001 John Wiley & Sons, Ltd.

KEY WORDS: die-swell flows; drag flow; free surface; simulations; stick-slip; viscoelastic

1. INTRODUCTION

Our earlier work involved Newtonian test case studies of planar and axisymmetric stick-slip and extrudate swell problems. Conditions with and without addition of drag flow were addressed, via a semi-implicit Taylor–Galerkin/pressure-correction finite element method (STGFEM) [1]. With an industrial flavour taking into account slip effects, the STGFEM was also used to compute solutions relevant to wire coating processes [2]. The present study, involving stick-slip and die-swell flows with elastic effects, is considered for the Oldroyd-B model with increasing Weissenberg (*We*) number. Hence, from a realistic fluid viewpoint, this benchmarking exercise is meant as a proving stage to the methodology, somewhat upstream of actual industrial flows. Creeping stick-slip flow (SSF) and die-swell flow (DSF) for axisymmetric and annular systems are explored and contrasted against theoretical solutions from the literature [3–7].

---

* Correspondence to: Institute of Non-Newtonian Fluid Mechanics, Department of Computer Science, University of Wales, Swansea, SA2 8PP, U.K.

Received January 2000
Revised August 2000

In such SSF and DSF, abrupt changes in boundary conditions arise, when velocity conditions at the wall adjust to stress conditions on the free surface. Following Crochet and Keunings [8], the Deborah number (*De*) is quoted as three times the *We* value for slit flows and four times for circular dies, the scale factors representing the ratio of maximum wall shear rate to average shear rate in fully developed entry flow.

These *benchmark* problems, of stick-slip and die-swell, are an excellent vehicle to address a phased study of such free-surface moving-boundary viscoelastic flows, prior to lunching into more complex and demanding problems. Our aim in this work is to establish our favoured fractional-staged approach within this flow regime. The benchmarks here are of the Maxwell/Oldroyd type, the choice being made for calibration purposes of the methodology with contrast to the theory and literature. The limitations on Weissenberg number solutions reported here, are a consequence of the model employed alone, and not the methodology. This is standard for the most proven schemes, currently accepted as state-of-the-art. On this point, we refer to our comments below and on other benchmarks for additional evidence, for example, under contraction flows past cylinders, Matallah *et al.* [9]. Our subsequent work in this area has progressed onto industrial-scale regimes of high shear and strain rates. This takes us into more complex wire-coating flows, with free-surfaces and drag flow, that calls upon more advanced constitutive modelling, with controlled extensional response through Phan–Thien/Tanner (PTT) models. There, Weissenberg numbers are not so limited and reach values of $O(10^3)$, see also Matallah *et al.* [10].

In the context of viscoelastic flow, with differential constitutive models, to achieve highly elastic solutions it is important to adopt specialized techniques, suitable to this task. To this end we employ consistent streamline upwinding and velocity gradient recovery. The particular treatment of the hyperbolic constitutive equation was initially presented in the STGFEM context by Carew *et al.* [11], who followed the pioneering investigations of Brookes and Hughes [12], and Shakib [13]. This deals with the consistent application and generalization of streamline-upwind/Petrov–Galerkin (SUPG) weighting to the problems of current interest. To attain still further accuracy and capture additional stability, velocity gradient recovery was advocated in Matallah *et al.* [9] The novelty of this method for viscoelastic incompressible flows lies in its combination of Taylor–Galerkin and pressure-correction schemes (see Hawken *et al.* [14]), with consistent streamline upwinding and velocity gradient recovery aspects (see also Szady *et al.* [15]). Further detail on this methodology and its variations is provided in Matallah [16]. Elsewhere, with this emerging methodology, we have solved complex fixed-boundary problems extensively. This has included three-dimensional flows in Baloch *et al.* [17,18], Hassager *et al.* [19], Ding *et al.* [20]; unsteady flows are reported in Tamaddon-Jahromi *et al.* [21,22]; and wire-coating flows are addressed in Mutlu *et al.* [23,24] and Matallah *et al.* [10,25].

The most competitive current methods in the viscoelastic area fall either into coupled (EVSS or EEME type) or fractional-staged approaches. The latter, our favoured option, offers the distinct advantage of tractability for large-scale complex flows, as large system matrices may be avoided in the solution process. In this categorization of schemes, we do not overlook, the transient issue, the aspect of continuous as opposed to discontinuous stress interpolation, lower levels of stress interpolation, or finite volume stress discretization. These scheme variants can be viewed as sub-classes. In the articles of Matallah *et al.* [9], and Wapperom and Webster

[26,27], these approaches were placed into context, and the full power and competitive level of this fractional-staged finite element formulation is brought to bear. Hence the current methodology is shown to be equally competitive with other approaches on accuracy and stability grounds, determined by reaching competitive levels of limiting Weissenberg numbers. Our motivation in the current articles is to take this methodology forward to deal with free-surface moving-boundary viscoelastic flows within this fractional-staged view of the system and its associated solution formalism.

In this article, we first present the setting of the governing equations and the details of the numerical scheme adopted. We point to the methodology applied successfully to free surface location and adjustment that maintains consistency. As surfaces are projected, special surface treatment with appropriate adjustments is required to ensure consistency throughout the solution procedure. For DSF, this allows for a study of variation in surface swelling profile as a function of increasing Weissenberg number. Theoretical results on swell and against other numerical solutions confirm the quality of present solutions for DSF. Comparison likewise is established for SSF against the theory. Following specification of the four base flows studied in Section 5, we document our results in Section 6, taking these in comparative form. Stick-slip reveals flow behaviour with increasing We, without the freedom of surface location. The impact of superimposing drag flow is investigated subsequently. The study then passes onto DSF, making the two-way comparison with SSF and against die-swell/drag flow. Our conclusions are recorded in Section 7. Converged solutions with Oldroyd-B are recorded up to a critical level of Weissenberg number, We^{lim}, beyond which instability sets in. For short-geometries and the streamline free-surface location method, the SSF limit reaches We^{lim} of 1.7 (to within 0.1), whilst for DSF solutions are obtained up to $We = 1.0$. These measures are improved upon with respect to the pressure-drop surface assessment method (see below) and the use of longer geometries.

2. BACKGROUND ON STICK-SLIP AND DIE-SWELL FLOWS

2.1. Stick-slip flow

Comparisons for SSF are made against the theoretical Newtonian solutions, of Trogdon and Joseph [3], who used a matched eigenfunction expansion method to calculate axisymmetric stick-slip and die-swell solutions for low-speed viscous flow with small surface tension in a two-dimensional cylindrical co-ordinate system. Agreement is found to be quite satisfactory.

Much of the work reported in the literature for SSF concentrates on the planar context. For present purposes and in order to extend to annular wire-coating situations, our interest here lies in studying axisymmetric, leading to annular configurations. Hence, strictly for planar SSF, we have the following to provide some guidance only.

Marchal and Crochet [28] performed calculations at high De for Oldroyd-B and Maxwell fluids using a mixed finite element method. An inconsistent streamline-upwind (SU) method was used to discretize the constitutive equation, and each element of the mesh was divided into bilinear sub-elements. This method is recognized as being overdiffusive, and only first-order accurate due to its variational inconsistency.

With Oldroyd-B fluids, Coleman [29] performed calculations for a range of Deborah numbers utilizing a boundary integral solution method. The maximum possible De^{lim} for stable converged solutions was found to be 2.6.

Owens and Phillips [30] presented solutions for a spectral domain decomposition method with an Oldroyd-B fluid. The spectral method required comparatively fewer degrees of freedom (dof) to describe the problem than its finite element counterparts. Deborah numbers up to 0.51 gave steady solutions, a De^{lim} similar to that found by Rosenberg and Keunings [31] with a streamline integration method.

Similarly, Baaijens [32] conducted numerical stability investigations with a discontinuous Galerkin method using a PTT model, incorporating monotonicity enforcement. The monotonicity was established by use of an implicit/explicit time discretization scheme, which led to convergence at high Deborah numbers. Of note is the fact that, the De^{lim} of 5.9 was achieved with stick length, $L_1 = 10$ units, for a stick:slip length ratio of 1/4, whilst for a ratio of unity, $De^{\text{lim}} = 1.85$. In addition, for an UCM model and longer geometry, where $L_2 = L_1 =$ 40 units the De^{lim} of convergence was 10. One should note here, that generally, considerably larger limits on Deborah numbers are commonly reported with PTT models, above those for the Maxwell/Oldroyd class.

Our results for axisymmetric SSF compare quite respectfully in form with those cited above.

2.2. *Die-swell flow*

The literature on die-swell studies offers the following. Tanner [4] presented an elastic-fluid theory for die-swell in long dies that provides guidance as to swelling ratios. Various finite element method (FEM) implementations for creeping die-swell Newtonian flows were discussed by Nickel *et al.* [33].

Chang *et al.* [34] were able to apply collocation and Galerkin methods to the slit and circular die swell flows for a generalized Maxwell fluid. The limits of Weissenberg number reached for slit and circular dies were 0.05 and 0.2 respectively.

Caswell and Viriyayuthakorn [5] presented Newtonian and viscoelastic finite element formulations, with a classical displacement (or u-v-p) method. For the viscoelastic calculations, a single integral Maxwell model and backtracking techniques were employed. Free surface profiles were estimated using a local uniform flow assumption nodes. Successful convergence to a Deborah number limit of 1.0 was achieved.

For Maxwell fluids, Bush *et al.* [6] presented planar and axisymmetric extrusion flow analyses using both finite element and boundary integral methods. This involved computation along streamlines. Limits of De for the finite element implementation were 1.5. The boundary integral formulation produced a lower De limit of 0.75 for the fine mesh employed, though this was increased to 1.0 upon further reducing mesh size by one half.

Similarly, predictions were reported by Crochet and Keunings [7], who documented results for an UCM fluid using a mixed finite element method with slit, circular and annular dies. These authors computed solutions to $De^{\text{lim}} = 0.75$ for slit flows and to $De^{\text{lim}} = 0.67$ for circular DSF. Crochet and Keunings [8] published further work on the slit flow with UCM fluids, concentrating on the importance of mesh refinement with respect to solution accuracy. This provided $De^{\text{lim}} = 1.25$ for slit flows and their finest meshes. The use of an Oldroyd-B fluid, allowed Crochet and Kennings [8] to increase De^{lim} for circular DSF beyond that reached with the Maxwell fluid, by as much as four times ($De^{\text{lim}} = 4.5$). In this study, both upstream and downstream lengths were 16 times greater than the channel radius.

Subsequently, Bush [35] made a detailed study into circular free-jet swelling behaviour for an Oldroyd-B model, with varying polymer concentration, represented through the viscosity fraction β (see Section 4.4.2). Comparisons between this viscosity fraction ($0.01 < \beta < 1.0$) and maximum possible Deborah number achieved ($2 < De^{\text{lim}} < 5$), were made upon a fine mesh. Likewise, Clermont and Normandin [36] provided an alternative stream tube method employing an integral constitutive model for the same problem. The stream tube method, roughly doubled the De values reached by Bush [35], though we note, that such a method lacks generality, being limited to streamline flows without recirculation.

3. GOVERNING EQUATIONS

For viscoelastic flow in the absence of body forces, the mass conservation and momentum equations are:

$$\nabla \cdot \mathbf{U} = 0 \tag{1}$$

$$\rho \mathbf{U}_t = \nabla \cdot \mathbf{T} - \rho \mathbf{U} \cdot \nabla \mathbf{U} - \nabla p \tag{2}$$

where variables velocity ($\mathbf{U}$), pressure (p), and extra-stress tensor $\mathbf{T}$ are defined over space and time, with temporal derivative represented as ($\mathbf{U}_t$) and density (ρ). The Cauchy stress tensor is defined through a unit tensor δ as

$$\sigma = -p\delta + \mathbf{T}$$

The Oldroyd-B model, attributed to Oldroyd [37], defines the relationship between the extra-stress $\mathbf{T}$ and rate of deformation tensor $\mathbf{D}$, *viz.*

$$\mathbf{T} + \lambda_1 \overset{\nabla}{\mathbf{T}} = 2\mu[\mathbf{D} + \lambda_2 \overset{\nabla}{\mathbf{D}}] \tag{3}$$

where

$$\overset{\nabla}{\mathbf{T}} = \mathbf{T}_t + \mathbf{U} \cdot \nabla \mathbf{T} - (\nabla \mathbf{U})^{\dagger} \cdot \mathbf{T} - \mathbf{T} \cdot \nabla \mathbf{U} \tag{4}$$

$$\mathbf{D} = \frac{1}{2}(\nabla \mathbf{U} + \nabla \mathbf{U}^{\dagger}) \tag{5}$$

$\overset{\nabla}{\mathbf{T}}$ is the upper-convected derivative of $\mathbf{T}$, $\mathbf{T}_t$ is the convected derivative of $\mathbf{T}$, $\mathbf{D}$ is the rate of strain tensor, $\overset{\nabla}{\mathbf{D}}$ is the upper convected derivative of $\mathbf{D}$, and material constants of shear viscosity μ, relaxation time λ_1 and retardation time λ_2, matrix transpose '†'.

Equation (3) contains $\overset{\nabla}{\mathbf{D}}$, with second-order spatial derivatives of the velocity field. For computational convenience, Crochet and Keunings [8] suggested reorganizing the extra-stress tensor $\mathbf{T}$, following Holstein [38], *viz.*

$$\mathbf{T} = \mathbf{T}_1 + \mathbf{T}_2 \tag{6}$$

$$\mathbf{T}_1 + \lambda_1 \overset{\nabla}{\mathbf{T}}_1 = 2\mu_1 \mathbf{D} \tag{7}$$

$$\mathbf{T}_2 = 2\mu_2 \mathbf{D} \tag{8}$$

Here, $\mathbf{T}_2$ is the Newtonian solvent stress with solvent viscosity μ_2; the elastic solute is $\mathbf{T}_1$ with solute viscosity μ_1. The relationship between viscosity, relaxation time, and retardation time is

$$\mu = \mu_1 + \mu_2 \quad \text{and} \quad \lambda_2 = \frac{\lambda_1 \mu_2}{\mu}$$

In this work the ratios of $\mu_1/\mu = 0.889$ and $\mu_2/\mu = 0.111$ are taken throughout.

Substitution and reorganization of the above into Equation (2), yields

$$\rho \mathbf{U}_t = \nabla \cdot \mathbf{T}_1 + 2\mu_2 \nabla \cdot \mathbf{D} - \nabla p - \rho \mathbf{U} \cdot \nabla \mathbf{U} \tag{9}$$

It is convenient to non-dimensionalize the system of equations employing characteristic length L and velocity V. Consequently, dimensionless quantities are taken of

$$r^* = \frac{1}{L} r, \quad Z^* = \frac{1}{L} Z, \quad \mathbf{U}^* = \frac{1}{V} \mathbf{U}, \quad p^* = \frac{L}{\mu_0 V} p, \quad \mathbf{T}^* = \frac{L}{\mu_0 V} \mathbf{T}$$

$$t^* = \frac{V}{L} t, \quad \nabla^* = L \nabla, \quad \frac{\mathrm{D}}{\mathrm{D}t^*} = \frac{L}{V} \frac{\mathrm{D}}{\mathrm{D}t}, \quad \lambda_1^* = \frac{V}{L} \lambda_\mathrm{i}, \quad \mu_i^* = \frac{1}{\mu_0} \mu_i$$

where μ_0 is a reference viscosity, and index $i = 1, 2$. For brevity, we may subsequently discard the * notation and assume this by implication. Taking elastic solute stress as τ, for an Oldroyd-B model, the system of Equations (1), (7) and (9), may be expressed non-dimensionally in the form:

$$\nabla \cdot \mathbf{U} = 0 \tag{10}$$

$$Re \mathbf{U}_t = \nabla \cdot (\tau + 2\mu_2 \mathbf{D} - p) - Re \mathbf{U} \cdot \nabla \mathbf{U} \tag{11}$$

$$We \tau_t = 2\mu_1 \mathbf{D} - \tau + We[\tau \cdot \nabla \mathbf{U} + (\nabla \mathbf{U})^\dagger \cdot \tau - \mathbf{U} \cdot \nabla \tau] \tag{12}$$

where $Re = \rho L V / \mu_0$, and $We = \lambda_1 V / L$ are non-dimensional group numbers, termed the Reynolds number, and Weissenberg number We, respectively.

4. NUMERICAL SCHEME

4.1. Discretization

The Taylor–Galerkin/pressure-correction finite element scheme [1,2,9] (as mentioned above) was the semi-implicit time-stepping procedure implemented to solve the Navier–Stokes equations (11) and stress equation (12). Taylor–Galerkin based algorithm is a fractional step method, that semi-discretizes first in the temporal domain, using Taylor series expansions in time, then a pressure-correction procedure to extract a time stepping scheme of second-order accuracy. A spatial Galerkin finite element method is used to complete the discretization. The flow domain is assumed to be discretized into a triangular mesh, with piecewise continuous linear (pressure) and quadratic (velocity) interpolation functions applying in such elemental regions. The three distinct fractional stages per time step the Taylor–Galerkin algorithm are:

Stage 1a

$$\frac{2Re}{\Delta t}(\mathbf{U}^{n+1/2}-\mathbf{U}^{n})=[\nabla\cdot(\tau+2\mu_2\mathbf{D})-Re\mathbf{U}\cdot\nabla\mathbf{U}-\nabla p]^{n}+\nabla\cdot\mu_2(\mathbf{D}^{n+1/2}-\mathbf{D}^{n}) \tag{13}$$

$$\frac{2We}{\Delta t}(\tau^{n+1/2}-\tau^{n})=[2\mu_1\mathbf{D}-\tau+We(\tau\cdot\nabla\mathbf{U}+(\nabla\mathbf{U})^{\dagger}\cdot\tau-\mathbf{U}\cdot\nabla\tau)]^{n} \tag{14}$$

Stage 1b

$$\frac{Re}{\Delta t}(\mathbf{U}^{*}-\mathbf{U}^{n})=[\nabla\cdot(2\mu_2\mathbf{D})-\nabla p]^{n}+[\nabla\cdot\tau-Re\mathbf{U}\cdot\nabla\mathbf{U}]^{n+1/2}+\nabla\cdot\mu_2(\mathbf{D}^{*}-\mathbf{D}^{n}) \tag{15}$$

$$\frac{We}{\Delta t}(\tau^{n+1/2}-\tau^{n})=[2\mu_1\mathbf{D}-\tau+We(\tau\cdot\nabla\mathbf{U}+(\nabla\mathbf{U})^{\dagger}\cdot\tau-\mathbf{U}\cdot\nabla\tau)]^{n+1/2} \tag{16}$$

where the time step index over the interval $[n, n+1]$ is denoted by n. The velocity and stress components are calculated at the half time step $(n+1/2)$ from data gathered at level n after Stage 1a and for Stage 1b, the intermediate velocity and stress component, $\mathbf{U}^*$ and $\mathbf{T}^*$, are solved for the full time step.

The two step predictor–corrector procedure provides the initial velocity and pressure fields, non-divergence-free $\mathbf{U}^{n+1/2}$ and $\mathbf{U}^*$ fields. The corresponding mass matrix governed equations are solved iteratively by a Jacobi method, using five iterations at most [14]. This may be implemented efficiently on an element-by-element basis, removing the system matrix storage overhead. Similarly, the stress equation is solved in Stages (1a and 1b) only.

Stage 2

$$\nabla^2(p^{n+1}-p^{n})=\frac{2Re}{\Delta t}\nabla\mathbf{U}^{*} \tag{17}$$

Using $\mathbf{U}^*$, via a Poisson equation over the full time step interval $[n, n+1]$, the pressure difference $(p^{n+1} - p^n)$ is calculated by a direct Choleski decomposition method. This is efficient for such a structured system, being sparse and banded.

Stage 3

$$\frac{2Re}{\Delta t}(\mathbf{U}^{n+1} - \mathbf{U}^*) = -\nabla(p^{n+1} - p^n) \tag{18}$$

Using $\mathbf{U}^*$ and pressure difference $(p^{n+1} - p^n)$, the non-divergent velocity field $\mathbf{U}^{n+1}$ is determined by Jacobi iteration. Galerkin weighting is adopted for all but the constitutive equation, that assumes the general SUPG form of $(1 + \alpha\mathbf{U}\cdot\nabla)\phi_i$, as discussed above (see Carew *et al.* [11]).

Velocity and stress interpolation is accomplished via quadratic basis functions ϕ_j over six-noded triangular elements, whilst linear basis functions ψ_k with three-noded triangular elements are used for pressure, *viz*.

$$(\tau_{rr}, \tau_{rz}, \tau_{zz}, \tau_{\theta\theta})^n = (\mathbf{T}_{1j}, \mathbf{T}_{2j}, \mathbf{T}_{3j}, \mathbf{T}_{4j})^n\phi_j \tag{19}$$

$$(V_r, V_z)^n = (\mathbf{U}_{1j}, \mathbf{U}_{2j})^n\phi_j \tag{20}$$

$$(p)^n = (\mathbf{P}_k)^n\psi_k \tag{21}$$

The convention of repeated indices implies summation throughout; index j is associated with vertex and mid-side nodes, whilst k is related to vertex nodes only.

After employing Equations (19)–(21), over domain Ω with non-overlapping finite element sub-regions, the fully discrete forms of Stages 1–3 become:

Stage 1a

$$\left[\frac{2Re}{\Delta t}\mathbf{M} + \frac{\mu_2}{2}\mathbf{S}\right](\mathbf{U}^{n+1/2} - \mathbf{U}^n) = \{-[\mu_2\mathbf{S} + Re\,\mathbf{N}(\mathbf{U})]\mathbf{U} - \mathbf{BT}\}^n + \mathbf{L}^\dagger\mathbf{P}^n \tag{22}$$

$$\frac{2We}{\Delta t}\mathbf{M}(\mathbf{T}^{n+1/2} - \mathbf{T}^n) = [2\mu_1\mathbf{M}(\mathbf{L} + \mathbf{L}^T) - \{\mathbf{M} + We\,\mathbf{N}(\mathbf{U})\}\mathbf{T} + We\{\mathbf{N}_1(\mathbf{T})\mathbf{L} + (\mathbf{N}_1(\mathbf{T})\mathbf{L})^\dagger\}]^n \tag{23}$$

Stage 1b

$$\left[\frac{Re}{\Delta t}\mathbf{M} + \frac{\mu_2}{2}\mathbf{S}\right](\mathbf{U}^* - \mathbf{U}^n) = \{-[\mu_2\mathbf{S} + Re\,\mathbf{N}(\mathbf{U})]\mathbf{U} - \mathbf{BT}\}^{n+1/2} + \mathbf{L}^\dagger\mathbf{P}^n \tag{24}$$

$$\frac{We}{\Delta t}\mathbf{M}(\mathbf{T}^{n+1} - \mathbf{T}^n) = [2\mu_1\mathbf{M}(\mathbf{L} + \mathbf{L}^T) - \{\mathbf{M} + We\,\mathbf{N}(\mathbf{U})\}\mathbf{T} + We\{\mathbf{N}_1(\mathbf{T})\mathbf{L} + (\mathbf{N}_1(\mathbf{T})\mathbf{L}^\dagger\}]^{n+1/2} \tag{25}$$

Stage 2

$$\frac{\Delta t}{2Re}\mathbf{K}(\mathbf{P}^{n+1}-\mathbf{P}^{n}) = -\mathbf{L}\mathbf{U}^{*} \tag{26}$$

Stage 3

$$\frac{2Re}{\Delta t}\mathbf{M}(\mathbf{U}^{n+1}-\mathbf{U}^{*}) = \mathbf{L}^{T}(\mathbf{P}^{n+1}-\mathbf{P}^{n}) \tag{27}$$

where variables notation references nodal vectors at time t^n for velocity ($\mathbf{U}^n$), stress ($\mathbf{T}^n$) and pressure ($\mathbf{P}^n$), intermediate non-solenoidal nodal velocity vector ($\mathbf{U}^*$); and matrices of mass ($\mathbf{M}$), momentum diffusive ($\mathbf{S}$), pressure stiffness ($\mathbf{K}$), advection ($\mathbf{N}$) and divergence/pressure gradient ($\mathbf{L}$).

The matrix notation employed above is defined as follows:

$$\mathbf{M}_{ij} = \int_{\Omega}\phi_i\phi_j \mathrm{d}\Omega$$

$$\mathbf{S} = \begin{bmatrix} S_{11} & S_{12} \\ S_{12}^{\dagger} & S_{22} \end{bmatrix}$$

$$(S_{11})_{ij} = \int_{\Omega}\left\{2\frac{\partial\phi_i}{\partial x_1}\frac{\partial\phi_j}{\partial x_1} + \frac{\partial\phi_i}{\partial x_2}\frac{\partial\phi_j}{\partial x_2} + \frac{\phi_i\phi_j}{r^2}\right\}\mathrm{d}\Omega$$

$$(S_{12})_{ij} = \int_{\Omega}\frac{\partial\phi_i}{\partial x_1}\frac{\partial\phi_j}{\partial x_2}\mathrm{d}\Omega$$

$$(S_{22})_{ij} = \int_{\Omega}\left\{\frac{\partial\phi_i}{\partial x_1}\frac{\partial\phi_j}{\partial x_1} + 2\frac{\partial\phi_i}{\partial x_2}\frac{\partial\phi_j}{\partial x_2}\right\}\mathrm{d}\Omega$$

$$\mathbf{N}(\mathbf{U})_{ij} = \int_{\Omega}\phi_i\phi_k\mathbf{U}_k\nabla\phi_j\,\mathrm{d}\Omega$$

$$\mathbf{N}_1(\mathbf{T})_{ij} = \int_{\Omega}\phi_i\phi_k\mathbf{T}_k\phi_j\,\mathrm{d}\Omega$$

$$\mathbf{B} = \begin{bmatrix} B_1 - B_3 & B_2 & 0 & B_3 \\ 0 & B_1 & B_2 & 0 \end{bmatrix}$$

$$(B_1)_{ij} = \int_{\Omega}\phi_i\frac{\partial\phi_j}{\partial x_1}\mathrm{d}\Omega$$

$$(B_2)_{ij} = \int_\Omega \phi_i \frac{\partial \phi_j}{\partial x_2}\, \mathrm{d}\Omega$$

$$(B_3)_{ij} = \int_\Omega \frac{\phi_i \phi_j}{r}\, \mathrm{d}\Omega$$

$$\mathbf{K}_{mn} = \int_\Omega \nabla\psi_m \nabla\psi_n \, \mathrm{d}\Omega$$

$$\mathbf{L} = (\mathbf{L}_1, \mathbf{L}_2), \qquad (\mathbf{L}_m)_{in} = \int_\Omega \psi_n \frac{\partial \phi_i}{\partial x_m}\, \mathrm{d}\Omega$$

where $\mathrm{d}\Omega = r\, \mathrm{d}r\, \mathrm{d}z$; $i, j, k = 1, 2, 3$; $m, n = 1, 2$; $x_1 = r$, $x_2 = z$.

In this formulation, there are various subtleties associated with boundary condition treatment of $\mathbf{U}^*$ and $(p^{n+1} - p^n)$, see Townsend and Webster [39], and Hawken *et al.* [14]. The natural conditions that emerge on the spatial gradient of $(p^{n+1} - p^n)$ may be taken as homogenous with a suitable selection of condition for $\mathbf{U}^*$. The time-stepping procedure is monitored for convergence to a steady state via relative increment norms (using both maximum and least squares measures) subject to satisfaction of a suitable tolerance criteria, taken here as 10^{-6}. Typical Δt is $O(10^{-4})$.

4.2. Streamline-upwind/Petrov–Galerkin (SUPG) method

The SUPG method has been shown to provide consistency uniformly in mesh size, while still retaining the advantages of enhanced stability and accuracy over Galerkin methods. For viscoelastic studies, the SUPG method has proved of great use in systems of high *We*, under the dominant, presence of the convective terms. By combination of the scalar multiplicative element dependent factor of the advective operator with the Galerkin test function, construction of the streamline upwinding weighting function is achieved:

$$w = \phi_i + \alpha^h \mathbf{U} \cdot \nabla \phi_i \tag{28}$$

On applying the above weighting function to each term in the differential equation, the consistent SUPG method emerges. A detailed study of the SUPG method for viscoelastic flow was made by Carew *et al.* [11], where the specification of the spatially dependent scalar parameter α^h is provided.

4.3. Gradient recovery

This technique is used in conjunction with the SUPG scheme, and involves recovery of velocity gradient fields (prior to solution of the stress field equations). This enhances the coefficients of the constitutive equation at the specified time stage, by smoothing ∇u. A number of local and global techniques can be used to capture smooth highly accurate discrete representations of the velocity gradient fields from the underlying finite element gradient approximations, produced at the element level. These continuous representations are compatible with the primary variables of the finite element solution, i.e. velocity, pressure, and stress.

The local direct method is the particular gradient recovery scheme chosen for this work (see Matallah *et al.* [9]), due to its attractive local compact properties and the avoidance of large matrix storage. Velocity gradient components generated for each element are local in nature, and therefore discontinuous from one element to another. For each quadratic triangular element, superconvergence at the mid-side nodes holds (Levine [40,41]). Velocity gradients are expressed in the form

$$G_k^e(x, t) = \frac{\partial \mathbf{u}}{\partial x_k}(x, t) \tag{29}$$

where $k = 1, 2$. Approximating the velocity vector, $\mathbf{u}(x, t)$ by finite element interpolation on each element renders u^h

$$u^h(x, t) = \sum_{j=1}^{N} \phi_j(x) u_j(t) \tag{30}$$

where N represents the number of nodes per element. By combining Equations (29) and (30), a direct calculation of the velocity gradients is possible thus:

$$G_k^{e,h}(x, t) = \sum_{j=1}^{N} \frac{\partial \phi(x)}{\partial x_k} u_j(t) \tag{31}$$

This procedure yields nodal gradient values per element. Direct averaging over elements for each nodal value then generates unique values, around which the quadratic continuous interpolation is based.

4.4. *Free surface location*

4.4.1. Numerical prediction. By implementing a free surface location method via a modified iterative technique, the extent of extrudate swell in a DSF may be determined (for example, in industrial casting processes). The following three boundary conditions may be defined on a free surface (Crochet *et al.* [42]):

$$v_r n_r + v_z n_z = 0 \tag{32}$$

$$t_r n_r + t_z n_z = S\left(\frac{1}{\rho_1} + \frac{1}{\rho_2}\right) \tag{33}$$

$$t_r n_z - t_z n_r = 0 \tag{34}$$

with variables specification of radial velocity (v_r), axial velocity (v_z), components of the unit normal to the free surface (n_r, n_z), surface force normal to the surface (t_r, t_z), principal radii of curvature (ρ_1, ρ_2) and surface tension coefficient (S).

A typical iterative approach for modelling a free surface flow involves enforcing the boundary conditions of Equations (33) and (34), see Reference [42]. The normal velocity is then calculated by Equation (32), which is used to describe the shape of the upper extrudate boundary for DSF (Figure 2). In the free jet flow, the distance from the axis of symmetry is:

$$r(z) = R + \int_{z=0}^{\infty} \frac{V_r(z)}{V_z(z)}\, \mathrm{d}z \tag{35}$$

where R is the tube radius. In this paper, the integral in Equation (35) is evaluated by Simpsons quadrature rule, thus providing an estimate of the extrudate shape. Free surface location is enforced every m (say 20) time steps of the field equations. Essentially, this leads to a form of sub-time steps over which boundary conditions and internal consistency is established.

In this manner, the location of the free surface may be specified, from which the swell and swelling ratio may be calculated. Comparison is made with Tanner's prediction [4] for swelling ratio ($\chi = R_j/R$, R_j is jet radius, R is tube radius, see Figure 2) and those from prior finite element calculations catalogued in Silliman and Scriven [43].

For superior accuracy on swell estimation, we have found it a most useful ploy to supplement the above streamline location method with a pressure-drop/mass balance surface assessment. This may then be invoked as a first estimate of the surface position at each *We* setting, commencing from a stick-slip scenario. Finally, we may perturb and validate the surface location calculated by use of the streamline method. Such an approach was found to yield considerably more stable and accurate solutions than achievable with the streamline technique alone. The pressure-drop/mass balance scheme is derived from the observation that a functional relationship holds at each level of *We*, between pressure-drop from the die at centreline and the swell generated. This may be observed from the profile patterns formed by pressure-drop (Δp) at centreline and swell (χ) for both SSF (without swell) to DSF (with swell). Using fitting procedures to samples our pressure-drop results, and with knowledge of the theoretical swell predictions, we empirically postulate the following relationship,

$$\chi = \frac{\Delta p(z, We)}{f(We)} \tag{36}$$

where

$$f(We) = 10.68 - 0.133\,We - 2.425\,We^2 \tag{37}$$

From such a relationship, the swell may be estimated numerically once the pressure-drop from the die has been computed. In this manner, one may proceed through an iterative or time-stepping process until a steady scenario is derived and consistency is ensured. This is rather reminiscent of the Caswell and Viriyayuthakorn [5] procedure. To achieve the very outer limits of Weisenburg number solutions, we have also used additional stress stabilization. For example, on the largest meshes and beyond $We = 1.5$, we have first solved each *We* stage, with vanishing surface extra-stress enforced. Once the surface has been estimated, these conditions may be relaxed.

4.4.2. Theoretical prediction. Theoretical predictions for free surface location in an extrusion process are compared during the scope of this investigation. Tanner [4] gives an elastic fluid theory of die-swell, which is based upon the principle of instantaneous elastic strain recovery after the fluid exits the die. The theory may be expressed as follows:

$$\chi = 0.13 + \left(1 + \frac{1}{2} S_{\mathrm{r}}^2\right)^{1/6} \tag{38}$$

where, S_{r} = recoverable shear and $S_{\mathrm{r}} = (N_1/2\tau_{rz})_{\mathrm{w}}$, N_1 = first normal stress difference, τ_{rz} = shear stress, $*_{\mathrm{w}}$ = values evaluated at die wall.

For a Poiseuille entry flow of an Oldroyd-B model

$$N_1 = \tau_{zz} - \tau_{rr} = 2\lambda_1\mu_1\dot{\gamma}^2, \quad N_2 = \tau_{rr} - \tau_{\theta\theta} = 0, \quad \tau_{rz} = (\mu_1 - \mu_2)\dot{\gamma}$$

so that

$$S_{\mathrm{r}} = \frac{\lambda_1\mu_1\dot{\gamma}_{\mathrm{w}}}{\mu_1 + \mu_2} = \beta De$$

where $\beta = \mu_1/(\mu_1 + \mu_2)$, $De = \lambda_1\dot{\gamma}_{\mathrm{w}}$, $\dot{\gamma}_{\mathrm{w}}$ = shear rate at die wall. This is the result we are able to utilize for comparison purposes below.

4.5. Surface solution reprojection

Nodal co-ordinates after the die-exit are modified to compensate for the free surface adjustment. Consequently, the velocity solution must be projected onto the new surface position (see Figure 1). This is accomplished as follows: two sample points are selected for each element at the mid-side (r_1, z_1) and vertex (r_2, z_2) node on the new surface positions, respectively. The total velocity magnitude, V_{total}, at the mid-side node of the boundary element must be maintained throughout the projection, where

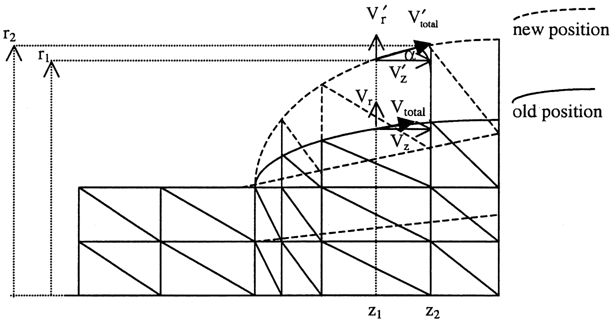

Figure 1. Free surface adjustment.

$$V_{\text{total}} = \sqrt{V_r^2 + V_z^2} \tag{39}$$

For the new free surface position, the tangent angle α to the boundary is

$$\alpha = \tan^{-1}\left(\frac{r_2 - r_1}{z_2 - z_1}\right) \tag{40}$$

Finally, the updated V_r' and V_z' velocity components must satisfy

$$V_r' = V_{\text{total}} \sin(\alpha) \tag{41}$$

$$V_z' = V_{\text{total}} \cos(\alpha) \tag{42}$$

This procedure is only necessary when surface adjustment is made after a time step-step, within the looping strategy commended above. Vertex nodes may be similarly adjusted to conform with forward oriented elements.

5. PROBLEM SPECIFICATION

5.1. Stick-slip flow (SSF)

The upstream and downstream parts of the die are classed as two distinct regions for stick-slip flow (SSF), with separate boundary conditions. The stick-slip condition assumes no-slip boundary conditions at the channel walls, adjusting to slip boundary conditions on exiting the die. Figure 2(a) illustrates these stick-sip conditions, where tangential velocity and shear stress vanish at the free surface, as well as the normal stress and cross-stream velocity at the outlet. An inlet Poiseuille flow and cylindrical co-ordinate system are applied within the analysis. Symmetry about the flow centreline is taken, permitting solutions to be sought over the upper half plane alone. Note that this implies a vanishing radial velocity at the fluid centreline z_1z_2. Dimensionless quantities involve a channel length and radius of one, and jet length of two. Here, channel radius and maximum inlet velocity are taken as characteristic scales of length and velocity respectively. Creeping flow conditions are approximated with a finite small Reynolds number of 10^{-4}, computing solutions upon a relatively fine mesh of 18×54 elements, 4033 nodes and 9111 dof (see Figure 3(a)), used in our prior mesh calibration studies of Reference [1]. With similar structure, longer geometries are also investigated, taking die length:jet length ratio as 0.5, but doubling each individual length. In addition, a die length:jet length ratio of 0.25 is attempted, with a die length of two units. This helps to distinguish the critical factor here to establish accurate solutions at the highest elasticity levels.

5.2. Stick-slip/drag flow (SSDF)

The more complex stick-slip/drag flow (SSDF) involves a pressure driven base flow at the inlet with a superimposed drag flow on the inner boundary (wire) that has finite radius. The remaining boundary conditions follow that of the previous stick-slip case. Figure 2(b)

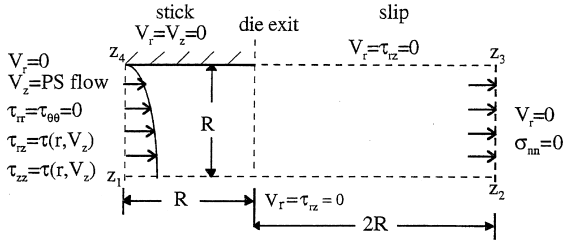

(a) **stick-slip**

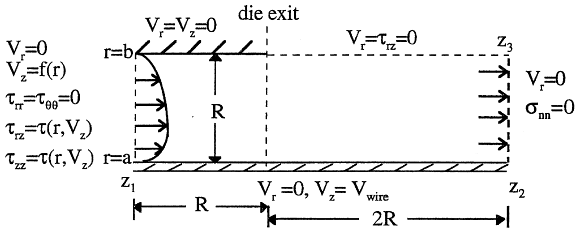

(b) **stick-slip/drag**

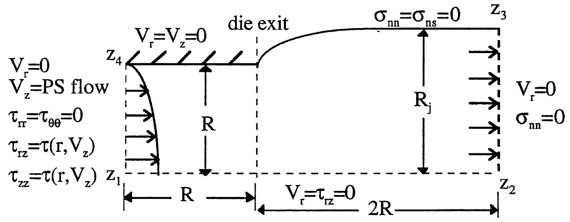

(c) **die-swell**

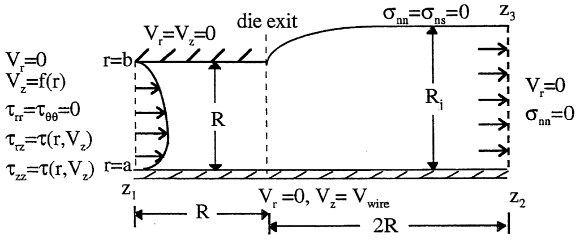

(d) **die-swell/drag**

Figure 2. Schema for flow problems.

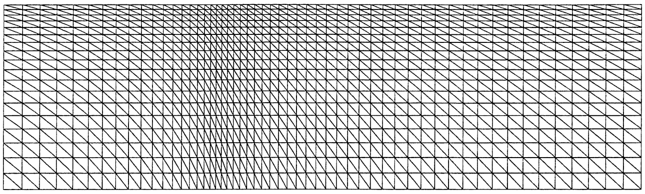

(a) **short mesh, 18×54 elements, die:jet length 0.5, jet length 2**

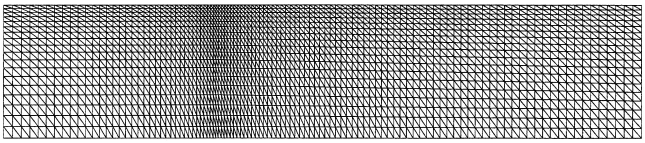

(b) **medium mesh, 18×108 elements, die:jet length 0.5, jet length 4**

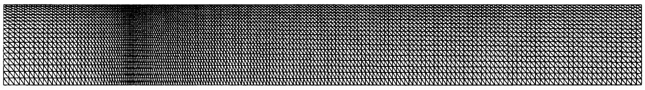

(c) **long mesh, 18×180 elements, die:jet length 0.25, jet length 8**

Figure 3. SSF: mesh patterns.

illustrates the annular inlet velocity V_z, defined in Appendix A, as well as the governing boundary conditions. The radial dimension of the moving wire is taken as 0.15 units. Characteristic scales are taken for length, as inlet hydraulic radius R, and for velocity, as with axisymmetric SSF. This leads to equivalent flowrates in both settings. Remaining dimensionless quantities are jet length of 2.0 units, wire speed of 0.5 units and positions z_1 and z_2 of -1.0 units and 2.0 units respectively. Here, the influence of drag flow may be analysed in the absence of free surface deformation.

5.3. Die-swell flow (DSF)

The die-swell flow (DSF) consists of two regions, one encompassing the shear flow within the die, governed by stick conditions at the boundary wall, and the other containing the extruded jet flow, where slip conditions at the free meniscus surface apply. A schematic illustration of the problem is provided in Figure 2(c), showing the inlet Poiseuille flow, channel length of unity; geometric locations z_1, z_2, and jet length are identical to the case of SSDF. Scales apply as for SSF. An initial mesh for die-swell instances is illustrated in Figure 13(a). In contrast to SSF, this flow demonstrates the influence of free surface deformation. Longer geometries follow, as above, in the case of SSF.

5.4. Die-swell/drag flow (DSDF)

This combination of the drag effects of SSDF, with the swell of the DSF model is shown in Figure 2(d). The inner boundary travels at the same speed as above with the SSDF of 0.5 units, and free surface boundary conditions remain as in the DSF case. Dimensionless quantities, characteristic velocity and length scales remain as in the DSF case above, with inlet annular V_z profile specified in Appendix A. Here, interest lies twofold; upon the introduction of drag flow to DSF and the contrast between die-swell and stick-slip in the presence of drag flow.

6. RESULTS AND DISCUSSION

6.1. SSF

The pressure and stresses for SSF are shown in Table I over a range of Weissenberg numbers. The Newtonian results ($We = 0$) are compared with the viscoelastic solutions of $0.25 \leq We \leq 1$. Radial velocities show little change for each We, with a 1 per cent increase at $We = 1$, while axial velocities remained unchanged. A sharp pressure increase with increasing We is observed at the singularity, with a 16 per cent increase at $We = 0.25$, rapidly building up to pressures three times that of the Newtonian case. All stress results are reported as total stresses inclusive of solvent contribution. Radial stresses display a highly localized exponential jump, reaching T_{rr} values ten times that for $We = 0$. Shear stress values indicate a general variation of 60 per cent while $T_{\theta\theta}$ stress values vary by 14 per cent, between Newtonian and viscoelastic fluids. The maximum attainable level of We^{lim} is 1.7 on short geometries, rising to 2.0 on the medium length mesh and 2.2 on the longest mesh (see Figure 3). Largest extra-stresses are axial and correspond to Weissenberg numbers between 0.25 and 0.5.

Following our separate mesh investigations of Reference [1], the refined mesh of 18 × 54 elements is used for all flow analyses covering Weissenberg numbers ranging from zero to

Table I. SSF: pressure and stress for various We.

Solutions		$We = 0$	$We = 0.25$	$We = 0.5$	$We = 0.75$	$We = 1$
P	min	−3.92	−0.57	−0.01	−0.01	0.00
	max	4.89	5.66	6.38	9.18	15.8
τ_{rr}	min	−3.49	−1.94	−1.84	−1.78	−1.95
	max	0.43	0.43	0.40	0.88	4.64
τ_{rz}	min	−7.23	−5.18	−4.53	−5.63	−4.56
	max	0.01	0.00	0.00	1.92	4.47
τ_{zz}	min	−1.07	−0.69	−0.57	−0.51	−2.79
	max	10.7	43.7	40.1	30.9	19.9
$\tau_{\theta\theta}$	min	0.00	0.00	0.00	0.00	0.00
	max	0.43	0.50	0.54	0.52	0.40

unity (Figure 3(a)). In the Newtonian instance, the velocity vector plot of Figure 4(a) depicts an initial Poiseuille flow changing to plug flow. The radial velocity contour plot gives the formation of a peak below the singularity, the highest velocity of 0.11 acting in the centre of the vortex. The axial velocity contour plot shows an increase at the top die wall, while the core flow slows down as it approaches the die exit (Figure 4(c)). A uniform pressure distribution is observed upstream of the die entry, tending to a negative singularity of -2.94 near the die exist (Figure 4(d)). The radial extra-stress and shear stress contours of Figure 4(e) and (f) represent negative stress concentrations at the die wall, with absolute minima at the singularity of -3.06 and -6.43, respectively. In contrast, a much tighter distribution of axial extra-stress occurs close to the singularity, with maxima of 10.7, as seen in Figure 4(g). The azimuthal stress of Figure 4(h) reflects a localized concentration of 0.43 on the centreline at the die exit station.

We now turn to results for SSF with the Oldroyd-B model at $We = 1$. Radial velocity profiles show a downstream distortion of the higher velocity region along the top boundary after the singularity, with the maximum velocity of 0.12, still located at the centre of the die exit flow (Figure 5(a)). The axial velocity contours of Figure 5(b) are much the same as for $We = 0$, except for a slight increase in the mid-velocity contour of 0.45. Figure 5(c) displays an initial linear pressure distribution, this time with a highly localized banding of positive pressure at the singularity point. The highest radial stresses (Figure 5(d)) are confined to the singularity region, as with shear stress (Figure 5(e)) of equal order. A localized high shear stress value of 4.47 is observed at the singularity. Non-vanishing T_{rz} persists further into the jet flow than in the Newtonian case. Axial extra-stress contour values of Figure 5(f) are larger than those for $We = 0$. High axial stress arises at the top boundary, particularly beyond the singularity, where stresses reach 19.9, almost double that for $We = 0$. The $T_{\theta\theta}$ extra-stress contours of Figure 5(g) for $We = 1$ are generally distorted and shifted downstream of the die, although stress extrema are more or less identical to Newtonian values.

The cross-channel upstream die and downstream jet radial velocity profiles for SSF and $We = 1$ are provided in Figure 6(a) and (b) respectively. Along the radial span $0 \leq r \leq 1$, the radial velocity increases initially, up to $z = 0.2$ (into the jet region), after which point it drops away. Also, the effect of the solution singularity is observed in the representation of the radial velocity gradient in the die exist neighbourhood. The axial velocity profiles of Figure 6(c) and (d) both show parabolic flow form, this time with maxima at the centre of the fluid. Upstream, the axial velocity diminishes in magnitude as it approaches the die exit, causing a suppression of the parabolic form. This effect is translated downstream (Figure 6(d)), where the parabolic axial velocity profile levels out to an almost linear state at $z = 0.8$. Stick-slip solutions for Weissenberg numbers ranging from zero to unity, are compared in their departure from the theoretical Newtonian solution in Figures 6(e)–(h), 7 and 8. A smooth parabolic radial velocity V_r, of the cross-channel velocity profiles, is seen to occur with much higher velocities achieved after the die exit than upstream (Figure 6(e) and (f)). The acuteness of the parabolic V_r profile flattens out somewhat with decreasing Weissenberg numbers, approaching that of the theoretical solution at $We = 0$, where the difference between maximum V_r values is approximately 4 per cent before the die exit, reducing to around 15 per cent in the jet region. It should be noted here that the relative solution size of V_r is an order of magnitude lower than V_z. Axial velocity (V_z) profiles upstream and downstream of the die are shown in Figure 6(g)

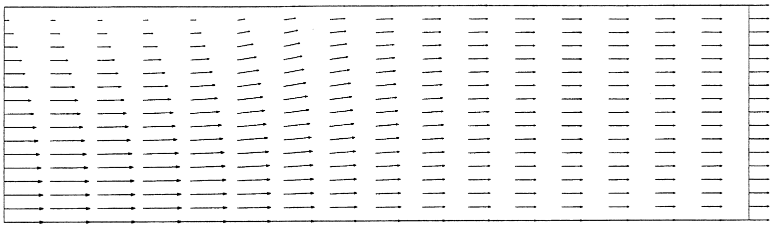

(a) **velocity vectors**

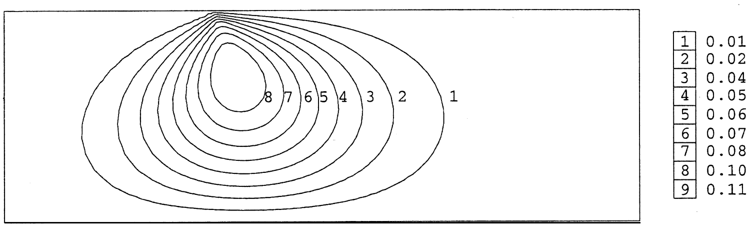

(b) **velocity V_r contours**

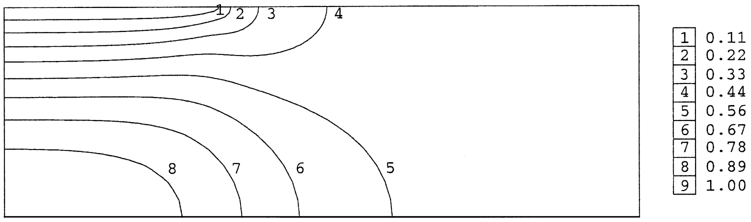

(c) **velocity V_z contours**

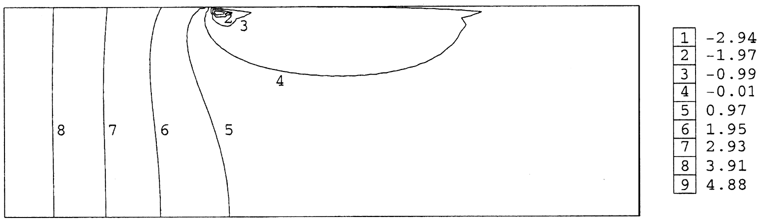

(d) **pressure contours**

Figure 4. SSF: short mesh, $We = 0$.

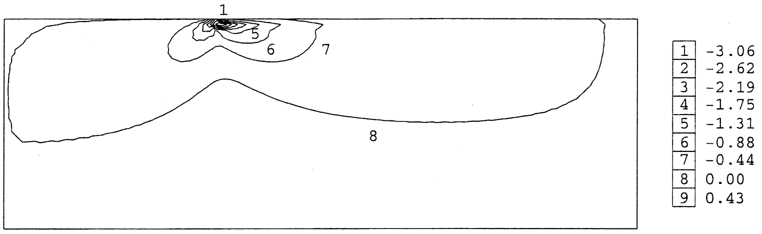

(e) stress T_{rr} contours

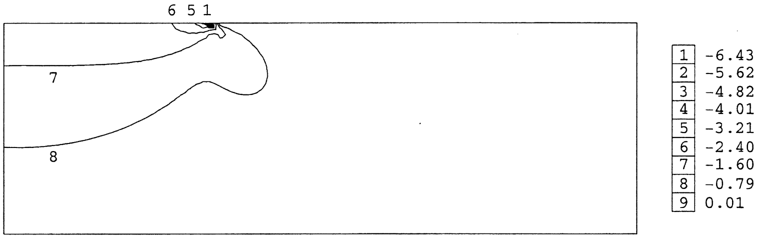

(f) stress T_{rz} contours

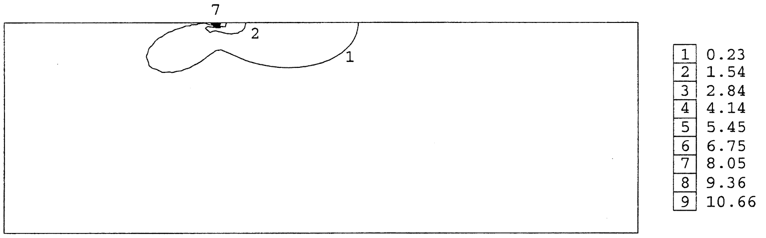

(g) stress T_{zz} contours

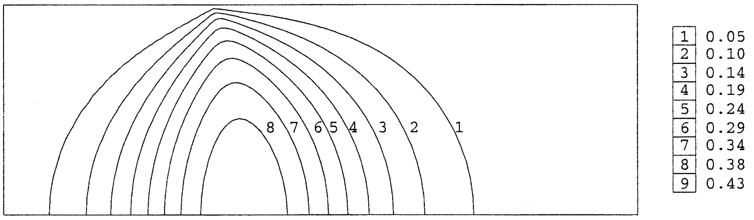

(h) stress $T_{\theta\theta}$ contours

Figure 4 (*Continued*)

and (h). Upstream profiles are parabolic, flattening out as maximum values appear near the die centre region (Figure 6(g)). The downstream V_z profile is of more complex curvilinear shape (Figure 6(h)). The $We = 0$ profile correlates closely with that of the theoretical result, the maximum difference from which occurs at the centreline of the fluid and ranges from approximately 0.1 per cent upstream to 3 per cent downstream of the die. The V_r velocity profiles of Figure 6(e) and (f) would appear to vary considerably between We values; however, inspection of the scale difference between V_r and V_z results reveals axial velocity variation twenty times greater than radial at the die centre. This difference is further magnified as the flow enters the jet region.

Shear rate I_2 profiles, where shear rate is represented as the second invariant of the rate of strain tensor, are compared for a range of Weissenberg numbers (Figure 7). The shear rate

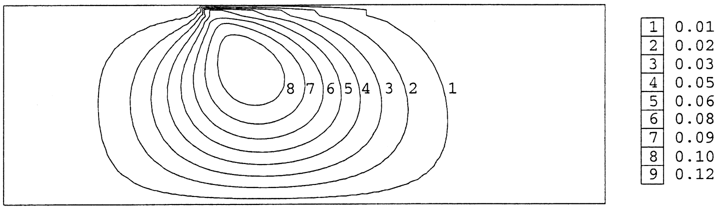

(a) **velocity V_r contours**

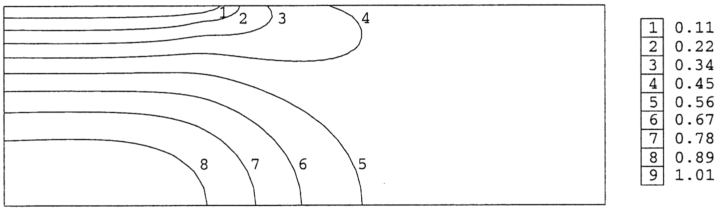

(b) **velocity V_z contours**

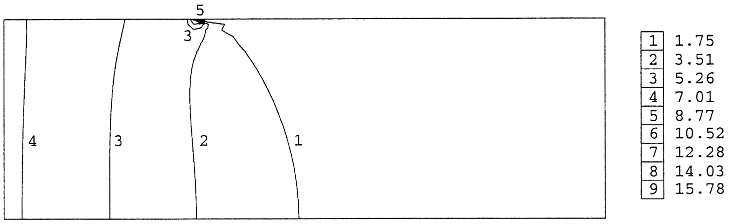

(c) **pressure contours**

Figure 5. SSF: short mesh, $We = 1$.

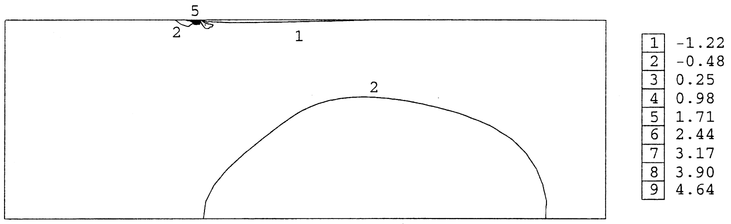

(d) stress T_{rr} contours

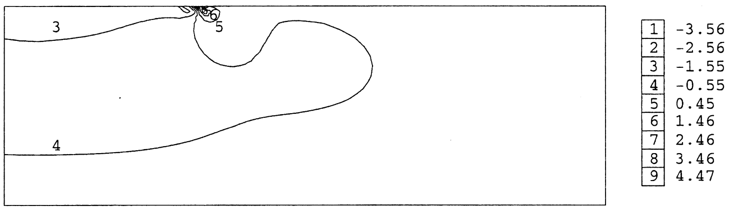

(e) stress T_{rz} contours

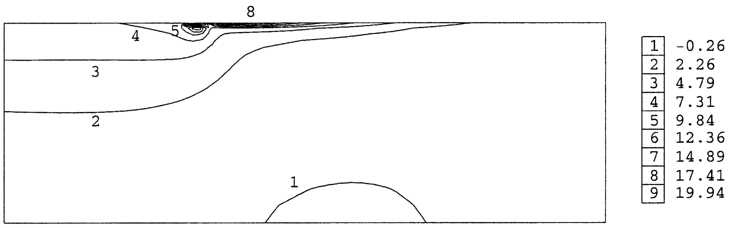

(f) stress T_{zz} contours

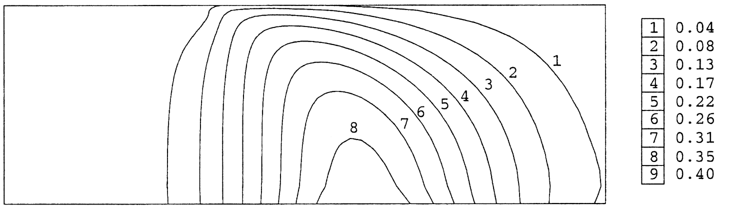

(g) stress $T_{\theta\theta}$ contours

Figure 5 (*Continued*)

peaks at the singularity region of the die-exit, and decay rates beyond the die become more gradual with increasing *We*. The decline in maximum I_2 from a value of 7.96 at $We = 0.25$ to 6.46 at $We = 1$ represents a drop of almost 25 per cent. Also, an undershoot in I_2 is noted, prior to the die exit at *We* of unity. This feature is not observed at earlier *We* values. Such rapid adjustments in I_2 surface values could signal the onset of flow instabilities.

The variation of pressure along the centreline of the die exit region for SSF is displayed in Figure 8(a). For all cases, a linear decline in pressure occurs upstream of the die exit location,

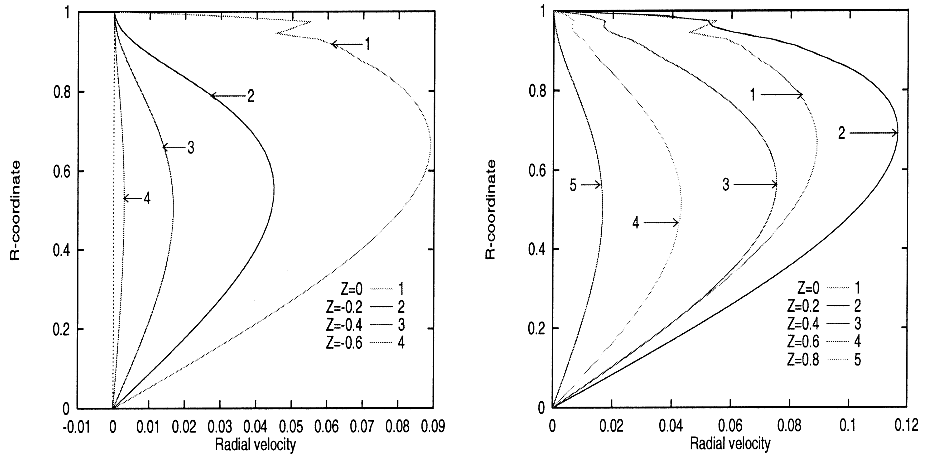

(a) V_r profiles, Z≤0

(b) V_r profiles, Z≥0

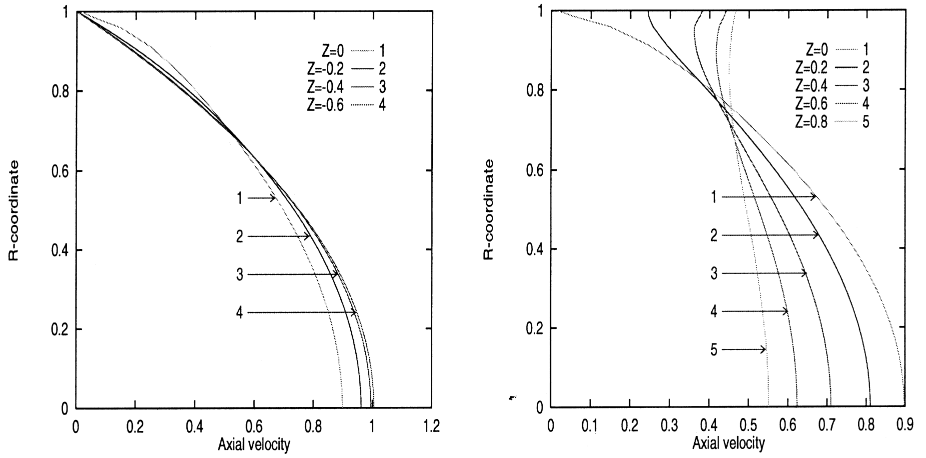

(c) V_z profiles, Z≤0

(d) V_z profiles, Z≥0

Figure 6. SSF: cross-channel velocity profiles, short mesh.

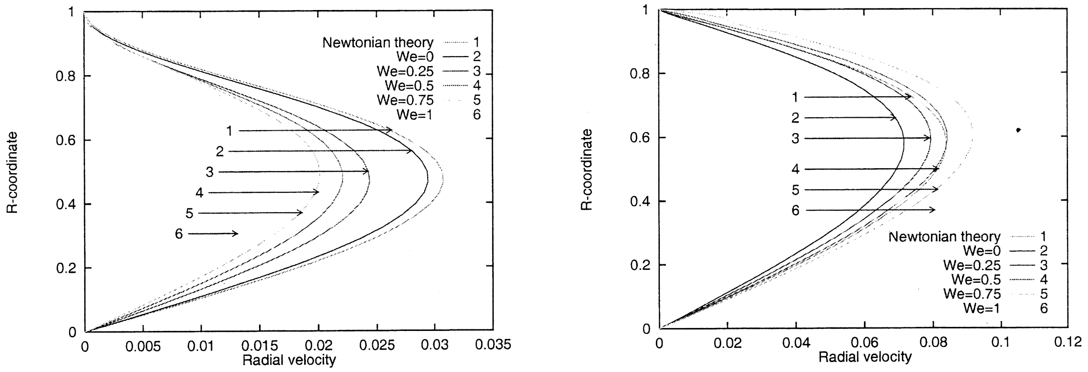

(e) V_r **profiles,** $0 \leq We \leq 1$, **Z=-0.4**

(f) V_r **profiles,** $0 \leq We \leq 1$, **Z=0.4**

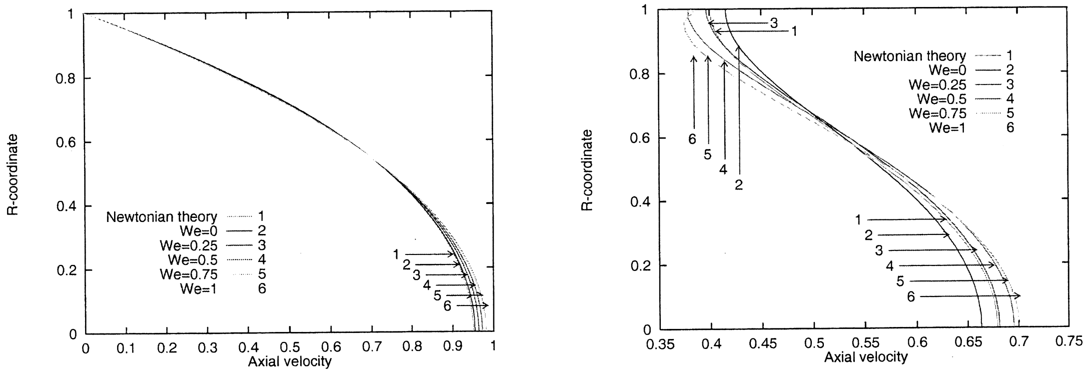

(g) V_z **profiles,** $0 \leq We \leq 1$, **Z=-0.4**

(h) V_z **profiles,** $0 \leq We \leq 1$, **Z=0.4**

Figure 6 (*Continued*)

after which the pressure reduction slows quadratically to zero at a distance of 1.5–2.0 from the die. There is close correlation with the theoretical result at the Newtonian limit, to within 5 per cent. Departure from this position is noted, with pressure drop increasing with increasing *We* from zero to unity. The normal stress invariant for various *We* is compared against the theoretical solution in Figure 8(b). Parabolic profile patterns are observed for all solutions, with minima close to the die exit in the jet region. Figure 8(c) shows the parabolic rise and fall of the radial stress component, as it passes through the die exit with minimum difference against the theoretical solution at $We = 0$, represented by a percentage error at the peak values of 4 per cent. The axial stress pattern of Figure 8(d) is almost a mirror reflection of the radial

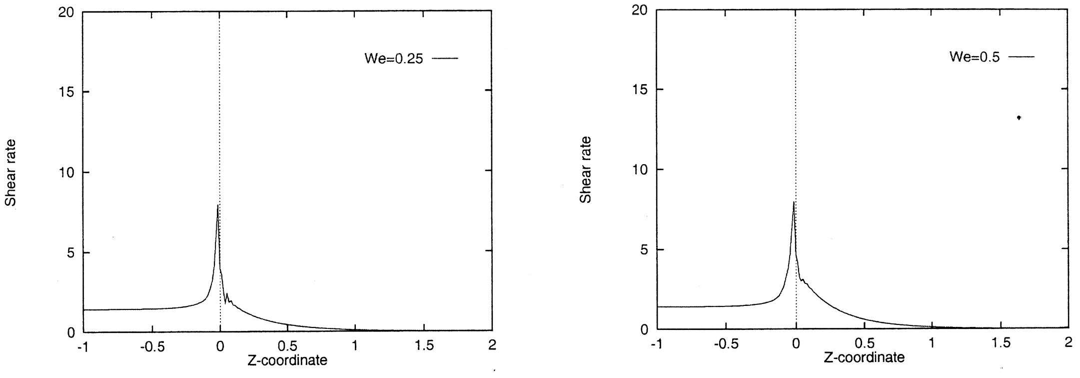

(a) We=**0.25**, I_2 **max=7.96**

(b) We=**0.5**, I_2 **max=8.00**

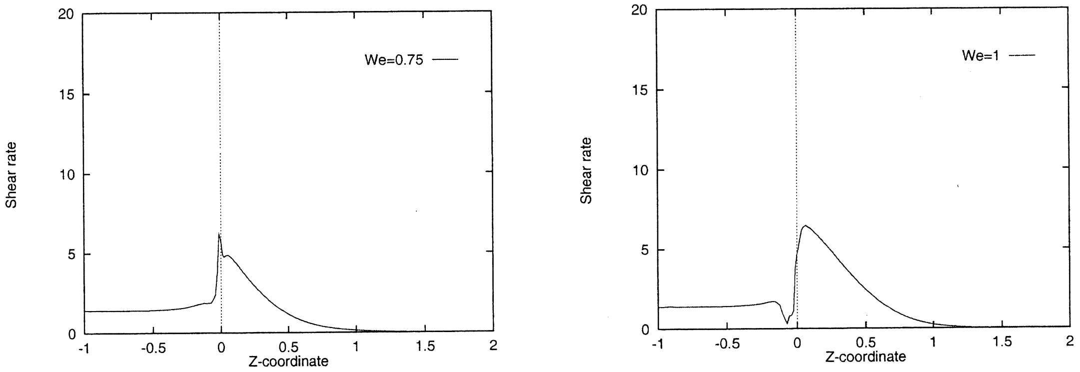

(c) We=**0.75**, I_2 **max=6.20**

(d) We=**1**, I_2 **max=6.46**

Figure 7. SSF: shear rate (I_2) on top surface, short mesh.

version, the familiar parabolic stress profile reaches a minimum value of -0.84 for $We = 0$, a difference of approximately 4 per cent from the theory.

6.2. SSDF

Table II provides results for SSDF at various Weissenberg numbers, illustrating extrema of pressure and stress, and departure from Newtonian values. Pressure and radial extra-stress increase exponentially with increasing We, reaching maxima of 22.2 and 7.06, three and 15 times greater than for the Newtonian case respectively. Maximum axial velocity V_z sustains a constant level at 0.82 for all values of We, whilst maximum radial velocity V_r varies by around 2 per cent.

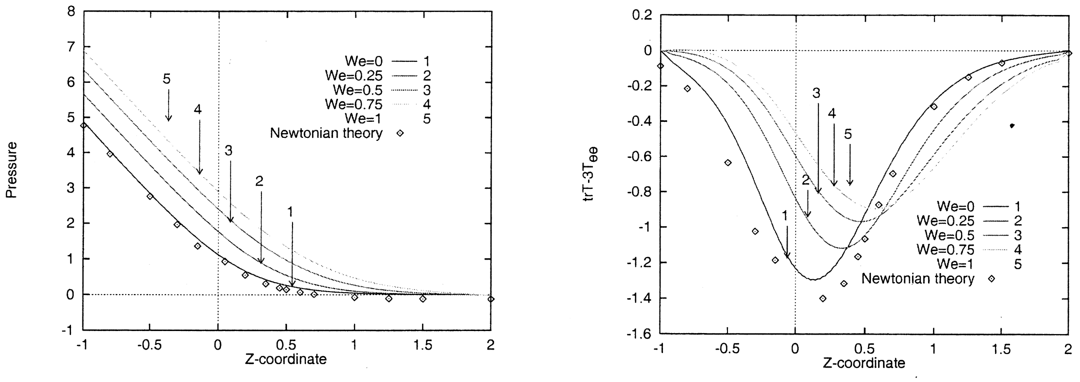

(a) **pressure** (b) $trT-3T_{\theta\theta}$

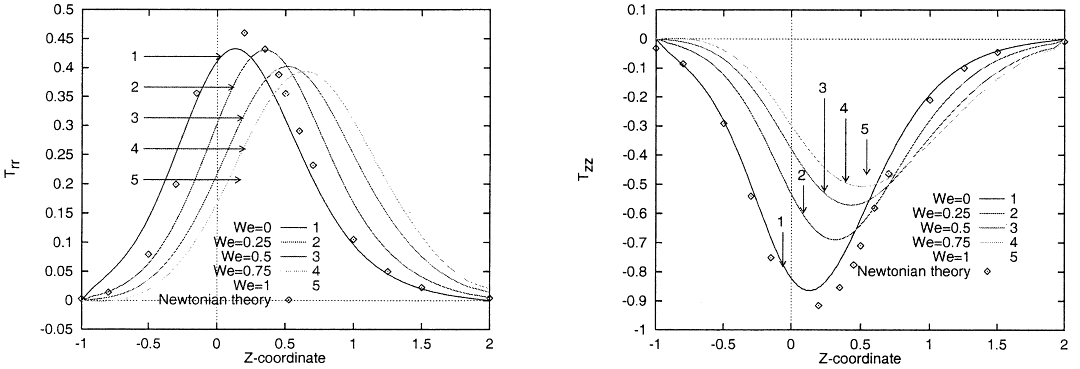

(c) **stress** T_{rr} (d) **stress** T_{zz}

Figure 8. SSF: line plot along axis of symmetry, various *We*, short mesh.

The same meshing as Figure 3(a) is employed for this flow instance up to $We=1$. The velocity vectors of Figure 9(a) demonstrates initial annular flow changing to plug flow on exit from the die. The radial velocity contours of Figure 9(b) are much the same as the stick-slip case of Figure 5(a), while the axial velocity is seen to increase at the top boundary (Figure 9(c)), once the fluid clears the die, where it maintains a steady value of 0.46. The upstream linear pressure profile (Figure 9(d)) of 9.58 decreases uniformly to the die exit, where a highly concentrated build up is observed at the singularity, reaching a peak of 22.2, 40 per cent higher than for pure SSF. A negative radial extra-stress persists throughout the flow (Figure 9(e)), except for a positive stress pocket of 7.06 at the singularity. Shear stress over the length of the top die wall remains negative until it reaches the singularity, where a dramatic jump in value to 5.82 occurs, before decaying to zero at the top extrudate boundary (Figure 9(f)). Axial stress T_{zz} at the lower boundary is understandably much higher than for the stick-slip problem

Table II. SSDF: pressure and stress for various *We*.

Solutions		$We=0$	$We=0.25$	$We=0.5$	$We=0.75$	$We=1$
P	min	-4.65	-0.25	-0.10	-0.26	-0.48
	max	7.06	8.04	8.90	16.3	22.2
τ_{rr}	min	-4.06	-2.34	-2.29	-2.21	-2.70
	max	0.48	0.47	0.44	3.93	7.06
τ_{rz}	min	-7.95	-4.83	-5.65	-7.04	-4.99
	max	3.02	3.12	3.12	4.38	5.82
τ_{zz}	min	-0.47	-0.58	-0.49	-0.42	-3.16
	max	12.1	55.8	52.8	32.3	22.8
$\tau_{\theta\theta}$	min	0.00	0.00	0.00	0.00	-0.01
	max	0.31	0.29	0.26	0.24	0.23

(Figure 5(f)) due to the influence of the moving lower boundary (wire) at the die centre, as depicted in Figure 9(g). However, extrema in axial stress of 22.83 and -3.16 still occur close to each other in the singularity neighbourhood. In contrast to SSF, the maximum $T_{\theta\theta}$ stress of 0.23 (Figure 9(h)) has shifted upward away from the lower free boundary into the core flow. This is a direct consequence of the additional drag force, imposed by the moving lower boundary.

Figure 10 demonstrates the SSDF cross-channel velocity profiles for $We=1$. The radial velocity profiles for half of the die, upstream and downstream of the die exit (Figure 10(a) and (b)) illustrate the rapid build up, followed by gradual reduction of the radial velocity as it passes through the die exit, accounting for the transition from parabolic to linear velocity fronts. On comparing the axial velocity profiles of Figure 10(c) and (d), with the stick-slip profiles of Figure 6(c) and (d), it is evident that the drag effects on the fluid have shifted the parabolic shape of flow profiles cross-stream. Maximum velocities are suppressed by approximately 10 per cent for the SSDF cases, with the velocity profile shape converging to a virtually linear shape at the end of the jet region ($z=0.8$).

Top surface shear rate I_2 profiles are illustrated in Figure 11 for increasing *We* values from 0.25 to unity. This figure contrasts with the situation as reported in Figure 7. Here, larger peak values are observed at the singularity at each *We* level over the stick-slip instance. The pre-die exit undershoot now occurs at the earlier stage of $We=0.75$. Peak values adjust from 10.76 at $We=0.25$ to 7.96 at $We=1.0$; a reduction of 26 per cent. There is a slight increase in I_2 maxima at $We=0.5$ over that at $We=0.25$, before decreasing with further increase in *We*.

Comparison of various profiles of stress, velocity, pressure and stress invariant at $We=1$ are made in Figure 12, between SSF and SSDF, midway across the top half of the die tube ($R=0.5$). This location was selected to analyse results in core flow. The radial velocity components at the die exit (Figure 12(a)) present parabolic profiles, whose maxima occur just after entry into the jet region. SSDF has a considerably smaller peak than SSF (a difference of 8 per cent) due to the suppressive effect on V_r of the moving boundary through the die. The axial velocity profile of Figure 12(b) reflects the opposite effect, but for the same reason, since the wire pulls the fluid through the die at a higher axial velocity. Figure 12(c) gives a 27 per cent increase in SSDF inlet pressure against that of SSF. The stress invariants of Figure 12(d) express a general 'wave' shaped profile. The initial invariant for SSF is at least double that for

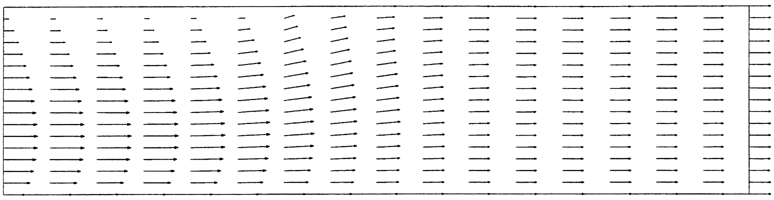

(a) **velocity vectors**

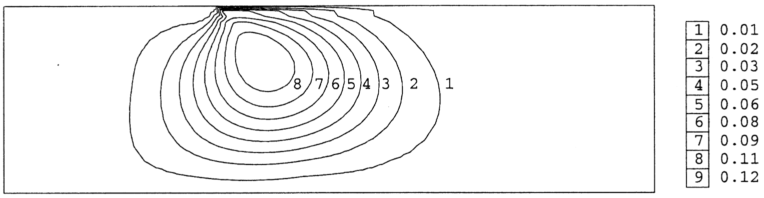

(b) **velocity V_r contours**

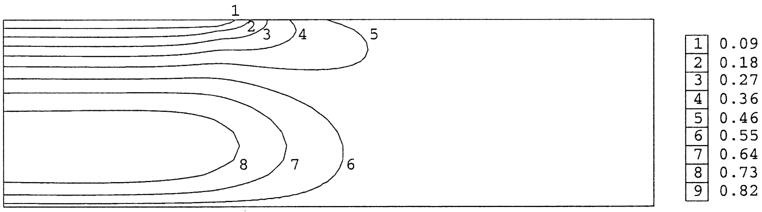

(c) **velocity V_z contours**

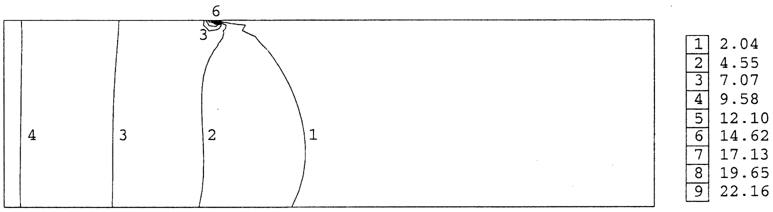

(d) **pressure contours**

Figure 9. SSDF, $We = 1$.

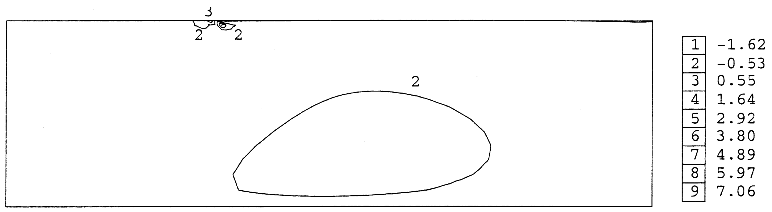

(e) **stress T_{rr} contours**

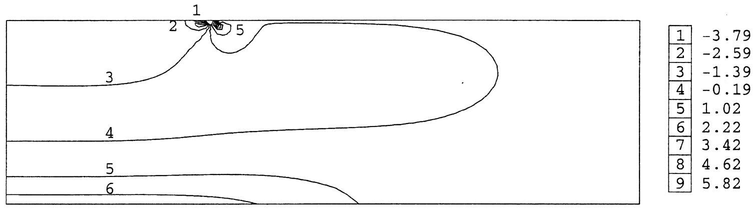

(f) **stress T_{rz} contours**

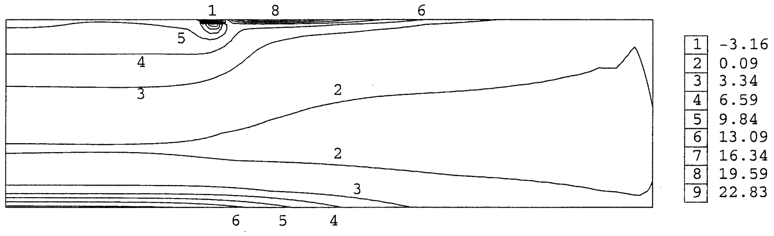

(g) **stress T_{zz} contours**

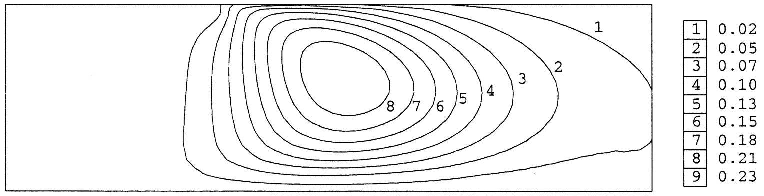

(h) **stress $T_{\theta\theta}$ contours**

Figure 9 (*Continued*)

SSDF, being due to the dominant influence of the invariant's T_{zz} component. This is reflected in Figure 12(g), where T_{zz} for SSDF is less than half that of SSF, due to the effect of the travelling wire aiding the fluids movement, therefore reducing internal axial stress. The radial extra-stress values (Figure 12(e)) give an almost opposite interpretation, with the SSDF case

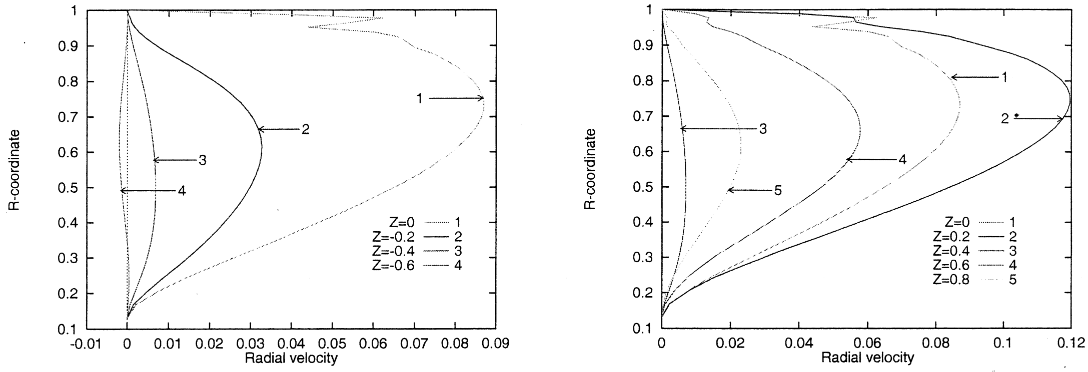

(a) V_r **profiles, Z≤0** (b) V_r **profiles, Z≥0**

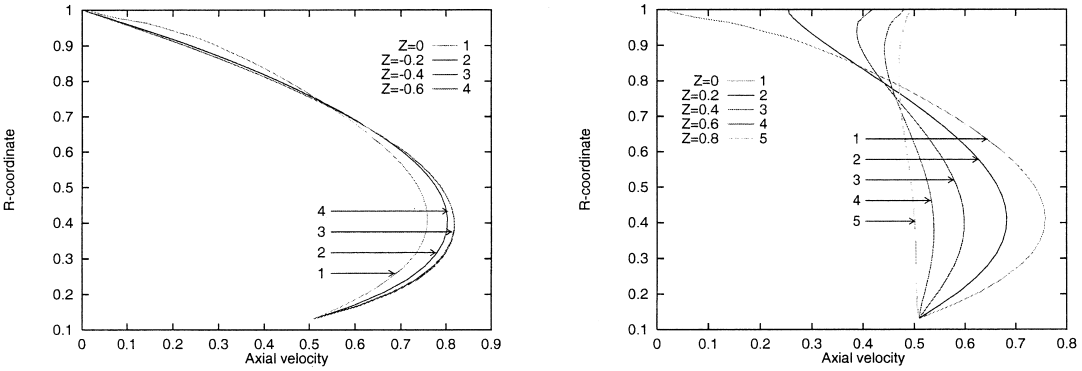

(c) V_z **profiles, Z≤0** (d) V_z **profiles, Z≥0**

Figure 10. SSDF: cross-channel velocity profiles, $We = 1$.

providing the dominant stress and peak values downstream of the die, approximately 40 per cent higher than for SSF. These high peak values are encountered when the fluid becomes free of the confines of the die wall. The shear stress T_{rz} profiles of Figure 12(f) demonstrate a gradient climb to vanishing T_{rz} at the far end of the jet region. This positive climb, and the fact that the SSDF is almost double SSF at the inlet, is due to the boundary influence upon the shear stress. As can be anticipated from Figure 12(h), $T_{\theta\theta}$ stress profiles over the die exit reflect a rapid increase in stress as the flow by-passes the singularity. The moving boundary of SSDF assists in dampening the $T_{\theta\theta}$ stress by approximately 27 per cent (at the peak value).

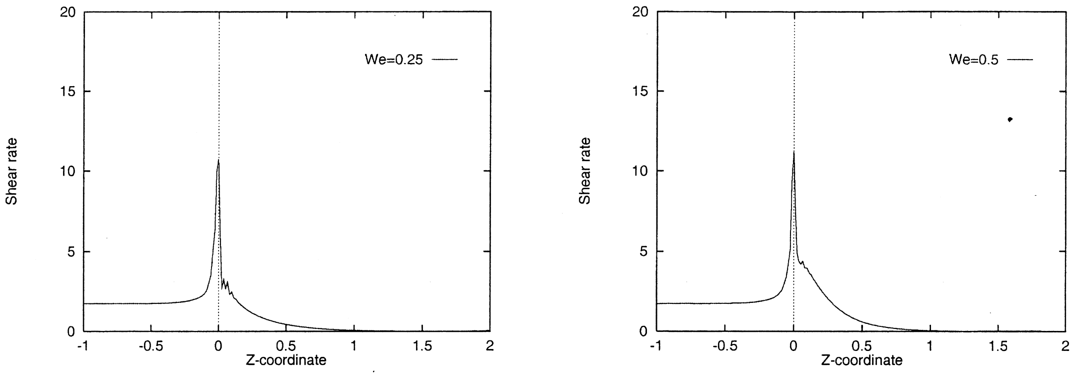

(a) We=**0.25**, I_2 **max=10.76** (b) We=**0.5**, I_2 **max=11.28**

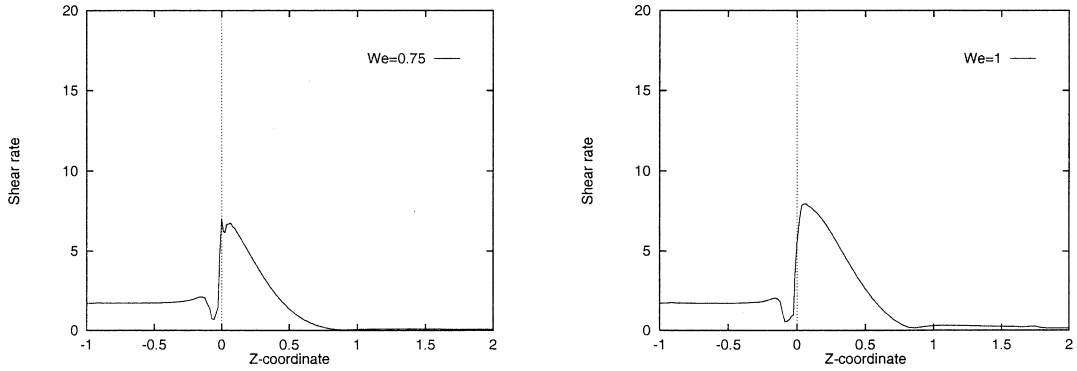

(c) We=**0.75**, I_2 **max=7.05** (d) We=**1**, I_2 **max=7.96**

Figure 11. SSDF: shear rate (I_2) on top surface.

6.3. DSF

The initial mesh used for DSF is illustrated in Figure 13(a). The velocity vector profile of Figure 14(a) reveals the gradual change from an inlet Poiseuille flow to an outlet plug flow. The radial velocity contour plot gives the typical peak formation at the die exit as for the other flow types, with maximum V_r of 0.20 occurring at the die centre (Figure 14(b)). The axial velocity contours of Figure 14(c) demonstrate a steady drop from 1.01 at the upstream die centre to 0.1 near the die wall boundary. Extrema in pressure and stress are recorded in Table III for DSF and increasing *We*. An extremely localized pressure pocket prevails at the singularity, reaching a peak value of 32.9 (Figure 14(d)), which is two and half times higher than for the SSF case. The radial extra-stress plot of Figure 14(e) also reflects a highly concentrated stress zone at the singularity of 12.6, over three times as severe as the stick-slip case of Figure 5(d). In contrast to the previous stick-slip (Figure 5(e) and (f)), there is upward distortion towards the free surface, yet similar trends in shear stress and axial extra-stress contour plots can be established (Figure 14(f) and (g)). Nevertheless, at the singularity, shear stress for die-swell reaches twice that for SSF. Figure 14(h) presents the typical build up of $T_{\theta\theta}$ stress at the centre of the die, reaching a maximum of 0.59 within the jet region.

Cross-channel velocity profiles for die-swell solutions at $We = 1$, in radial and axial component forms, are provided in Figure 15(a)–(d). The upstream and downstream radial velocity profiles for die-swell exhibit similar behaviour to that of SSF (Figure 6(a) and (b)), with the exception of a slightly stronger upstream velocity profile (approximately 30 per cent

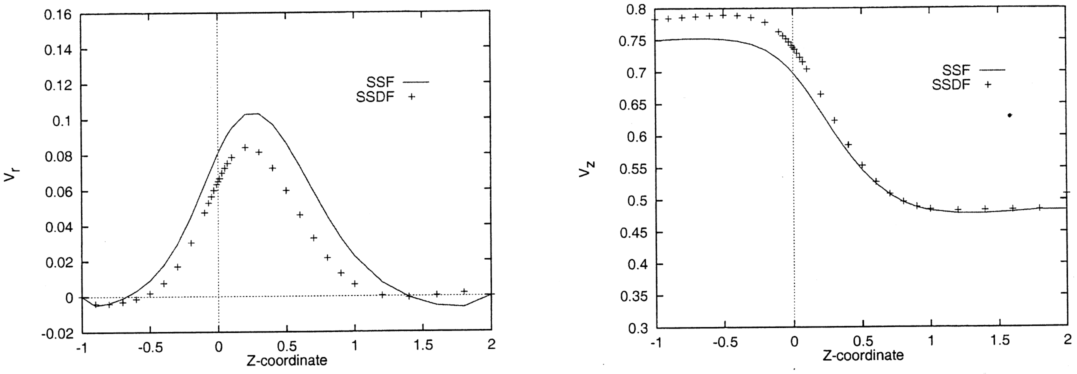

(a) **velocity** V_r

(b) **velocity** V_z

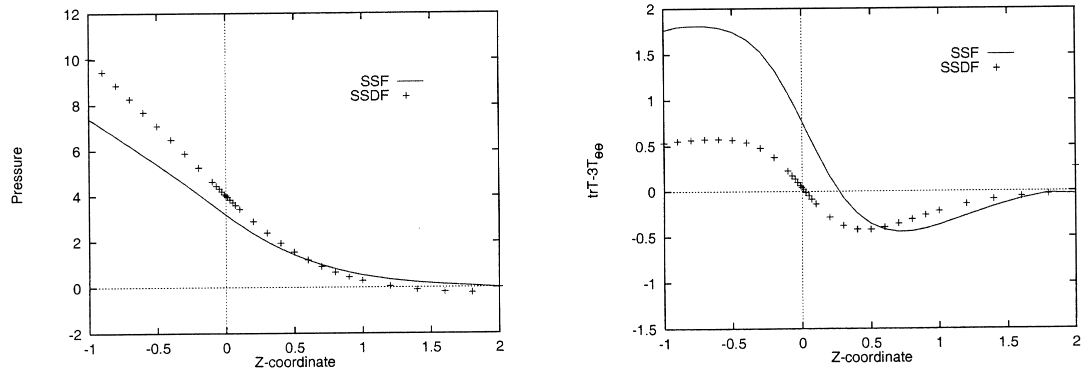

(c) **pressure**

(d) $trT - 3T_{\theta\theta}$

Figure 12. SSF and SSDF: line plot along horizontal line $R = 0.5$, $We = 1$.

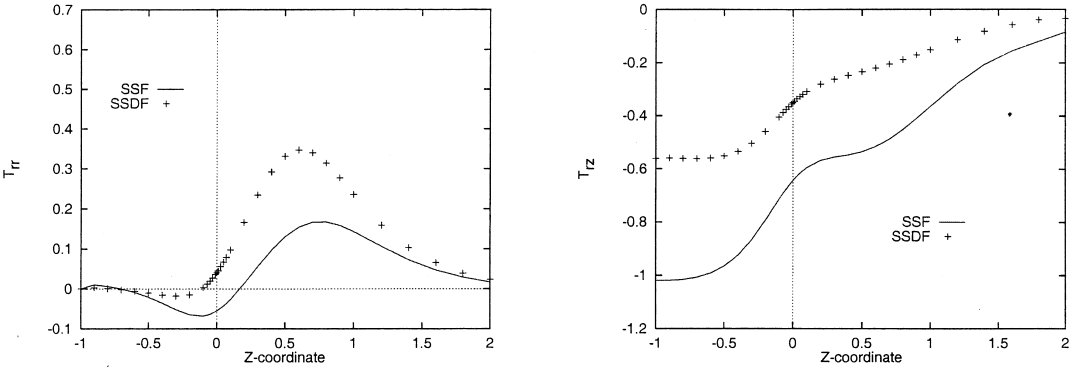

(e) **stress** T_{rr} (f) **stress** T_{rz}

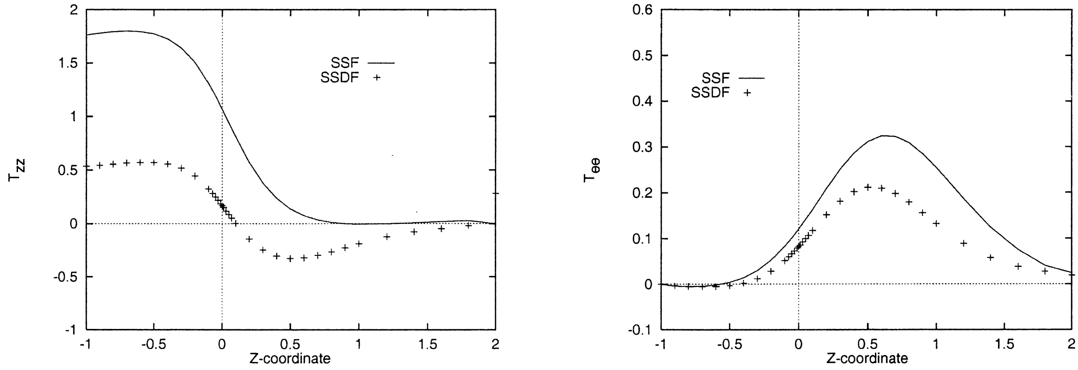

(g) **stress** T_{zz} (h) **stress** $T_{\theta\theta}$

Figure 12 (*Continued*)

increase) at the die exit in the die-swell instance. The downstream flow exhibits a considerable increase in maximum radial velocity (compared with that for SSF), of almost 40 per cent before trailing off to a maximum velocity of 0.068 at $z = 0.8$ beyond the die. The external free surface swell is obviously responsible for this increase. The difference between the die-swell and the previous SSF is less apparent in the axial velocity V_z profiles (Figure 15(c) and (d)) than for the former V_r component. The only difference worthy of note is in the die-swell jet region, where for each recorded reading a slightly weaker axial velocity occurs at the centre of the fluid. Figure 15(e)–(h) record the DSF solutions with increasing *We*, through cross-channel radial and axial velocity profiles for positions $z = -0.4$ and $z = 0.4$ upstream and downstream of the die. Weissenberg numbers range from zero to unity, the limit for steady solutions. The parabolic radial velocity profiles increase in magnitude with decreasing *We* in the upstream

Table III. DSF: pressure and stress for various *We*.

Solutions		$We=0$	$We=0.25$	$We=0.5$	$We=0.75$	$We=1$
P	min	-7.10	-1.90	-1.22	-0.95	-0.68
	max	4.94	5.59	14.5	24.7	32.9
τ_{rr}	min	-4.38	-1.70	-1.24	-0.69	-0.89
	max	0.52	2.25	3.52	7.54	12.6
τ_{rz}	min	-9.01	-4.00	-8.66	-6.67	-4.05
	max	0.94	11.4	8.11	7.96	9.48
τ_{zz}	min	-1.03	-0.71	-0.59	-6.41	-5.96
	max	15.1	40.5	23.8	20.8	19.6
$\tau_{\theta\theta}$	min	0.00	0.00	-0.01	-0.01	-0.01
	max	0.52	0.49	0.51	0.53	0.59

section. On exit of the die the converse is true (Figure 15(e) and (f)). Parabolic profiles of the upstream axial velocity are observed in Figure 15(g) that vary little in velocity maxima over the full range of Weissenberg numbers. As the axial velocity enters the jet region (Figure 15(h)) there is a decrease in maximum velocity of about 30 per cent. Variation between each *We* profile is more pronounced in this component, with the greatest variations near the free surface, where the flow disturbance due to the singularity is most prominent.

The top boundary shear rate plots of Figure 16 show an initial inlet constant value of 1.4, increasing exponentially upon nearing the singularity to a peak of 14.0 for the lowest *We* value of 0.25. This peak can be seen to first marginally increase to 12.3 and then diminish with increasing magnitude of *We*, to an ultimate peak value of 7.19 at $We=1$. Comparing DSF with the SSF case of Figure 7, a sharper reduction in post-die shear rate is observed for DSF; as well as more elevated peaks in shear for $We<1$. Oscillations in profile are apparent beyond $We=0.5$ as the singularity is transcended. I_2 pre-die exit undershoot is observed at this stage and subsequently; earlier therefore in *We* than for SSF. A post-die exit minimum also arises beyond $We=0.75$, not present in stick-slip. Oscillation in I_2 at $We=1$ could indicate the imminent onset of instability.

The die-swell pressure distribution along the axis of symmetry for various Weissenberg numbers is shown in Figure 17(a), and follows those observed for SSF (Figure 8(a)). Comparing with the stick-slip case, a substantial increase in the normal stress invariant minima of 15 per cent occurs for $We=0$ (Figure 17(b)). The radial extra-stress component profiles display some dramatic behaviour, with stress increasing to a peak of 0.6 with increasing Weissenberg number (Figure 17(c)), opposite to that of the stick-slip case. A tighter formation of curves for the die-swell axial extra-stress is observed in the jet region (Figure 17(d)) above that in the die, with the minimum T_{zz} value reaching -1.0, a reduction of about 12 per cent.

Comparing SSF with DSF at the mid-top half of the tube ($R=0.5$, $We=1$) over the die exit region reveals some marked differences. The radial velocity variations of Figure 18(a) show the familiar shaped profile of Figure 12(a) for SSF. The flow swelling characteristics of the DSF

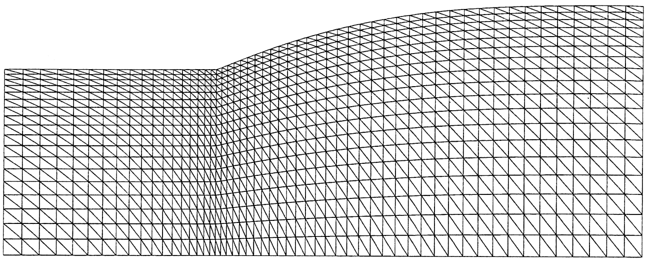

(a) **short mesh, 18×54 elements, die:jet length 0.5, jet length 2**

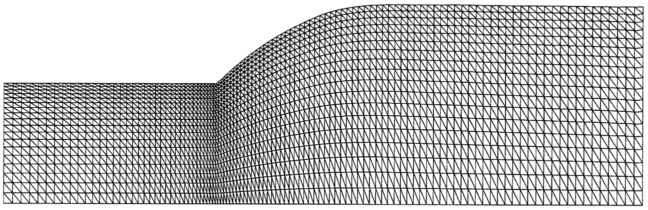

(b) **medium mesh, 18×108 elements, die:jet length 0.5, jet length 4**

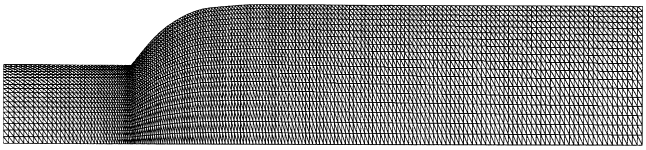

(c) **long mesh, 18×180 elements, die:jet length 0.25, jet length 8**

Figure 13. DSF: mesh patterns.

are responsible for the 23 per cent increase in V_r (comparing with SSF). Understandably, the radial increase in diameter for the DSF as it enters the jet region, would cause a corresponding reduction in axial velocity. The reduction in V_z to 60 per cent that of SSF is apparent in Figure 18(b). The external fluid volume increase for DSF also aids the reduction in pressure drop beyond the die (Figure 18(c)). Upstream normal stress invariant characteristics remain more or less the same for SSF and DSF. However for DSF, the more extreme drop of invariant on exiting the die (Figure 18(d)) is mostly due to the reduction in V_z within this region. This effect is also observed in the stress component T_{zz} that dominates the invariant (Figure 18(g)). The radial stress T_{rr} profiles over the die exit are shown in Figure 18(e). Again, the swelling phenomena of DSF results in a dramatic peak in T_{rr}, approximately 45 per cent higher than that of SSF. Reduction in shear stress T_{rz} as the flow exits the die is similar for both flow types. The slightly faster reduction in T_{rz} for DSF is generally due to the more rapid kinetic

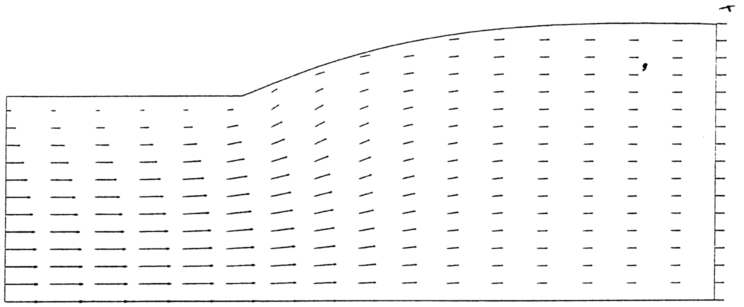

(a) velocity vectors

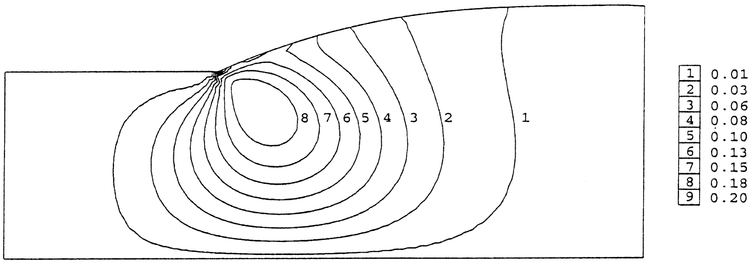

(b) velocity V_r contours

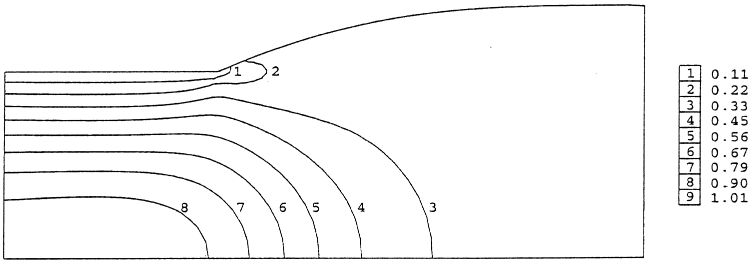

(c) velocity V_z contours

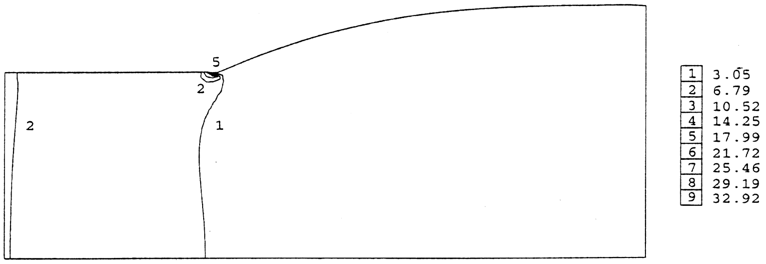

(d) pressure contours

Figure 14. DSF: short mesh, $We = 1$.

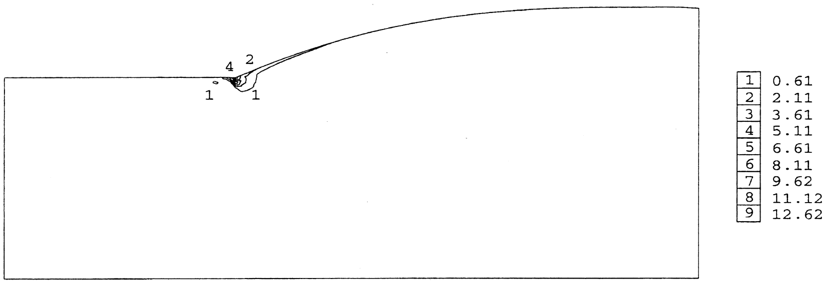

(e) **stress τ_{rr} contours**

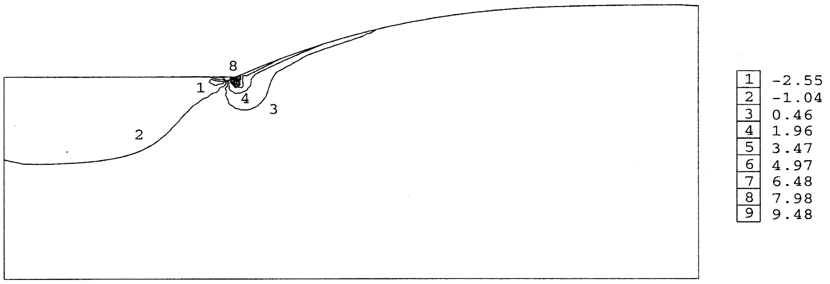

(f) **stress τ_{rz} contours**

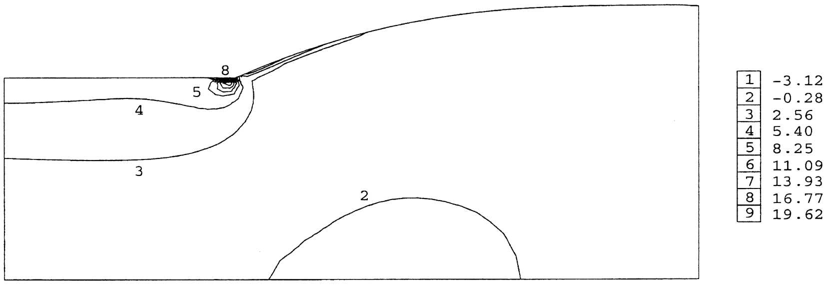

(g) **stress τ_{zz} contours**

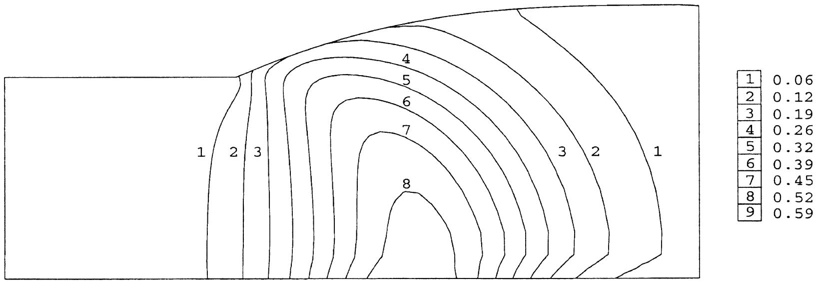

(h) **stress $\tau_{\theta\theta}$ contours**

Figure 14 (*Continued*)

energy loss from the swelling effects (Figure 18(f)). The $T_{\theta\theta}$ parabolic shape and peak (see Figure 18(h)) on exiting the die can mainly be attributed to the radial velocity behaviour, though the axial velocity has some influence also. Hence, the reason for the 30 per cent increase in DSF stress at $z = 0.7$.

Figure 19(a) plots the centreline velocity as a function of axial distance from the die exit in contrast to the literature. The velocity profile result for the Newtonian STGFEM follows closely the results of a similar FEM Newtonian study provided by Casewell and Viriyayuthakorn [5]. The Newtonian STGFEM solution is seen to have a less steep velocity profile at the transition from Poiseuille flow to uniform plug flow, in contrast to those for either a Maxwell [5] or Oldroyd-B (STGFEM) fluid model. When contrasting to the literature (in Figures 19–21 and Table IV), results are charted against Deborah number by convention, where for current scales $De = 2We$. The pressure distribution of the Newtonian jet flow along

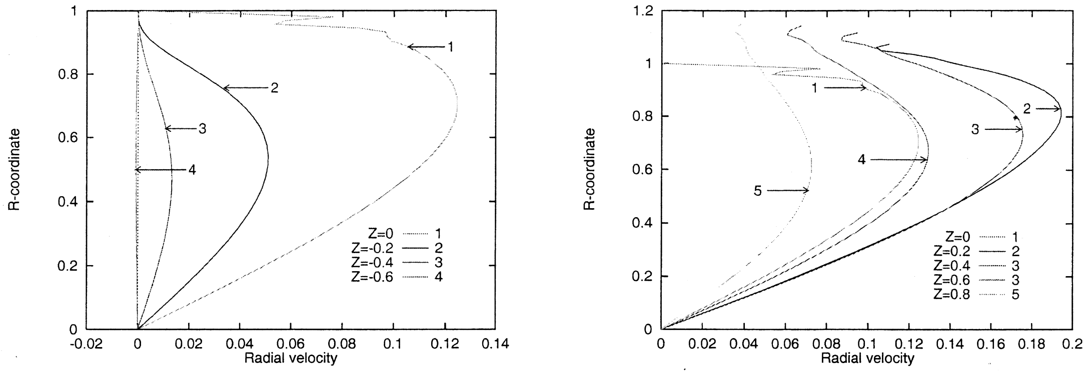

(a) V_r **profiles, $We=1$, Z≤0** (b) V_r **profiles, $We=1$, Z≥0**

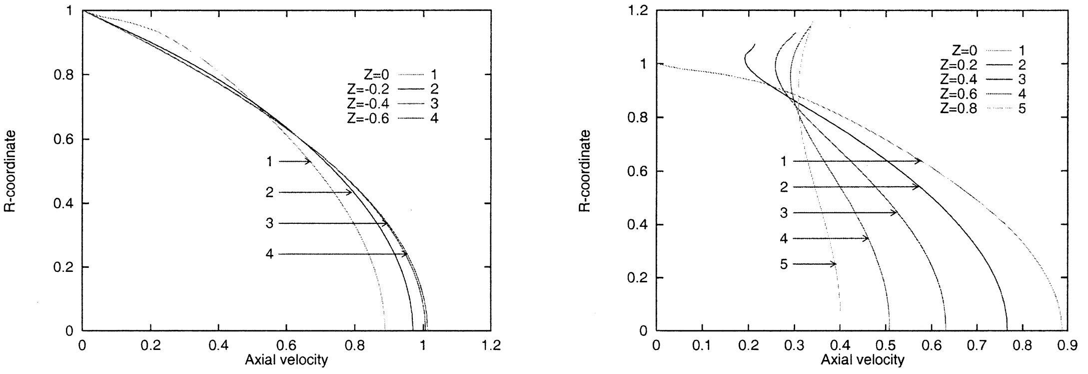

(c) V_z **profiles, $We=1$, Z≤0** (d) V_z **profiles, $We=1$, Z≥0**

Figure 15. DSF: cross-channel velocity profiles, short mesh.

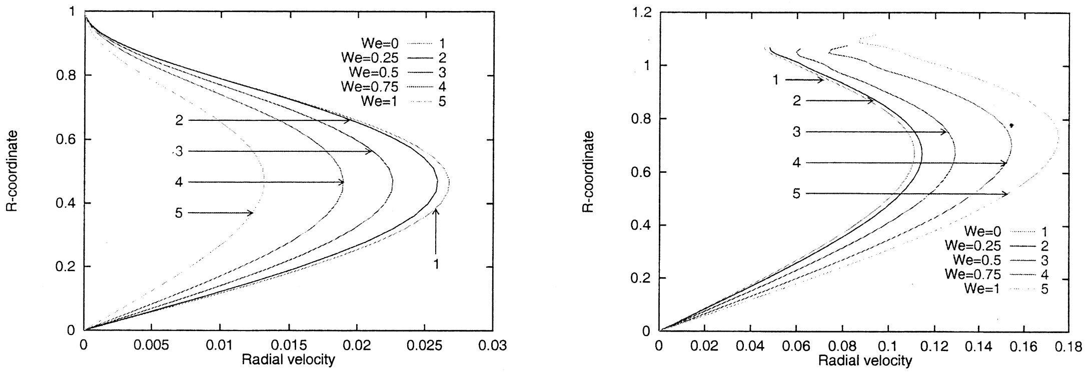

(e) V_r **profiles,** $0\leq We \leq 1$, **Z=-0.4** (f) V_r **profiles,** $0\leq We \leq 1$, **Z=0.4**

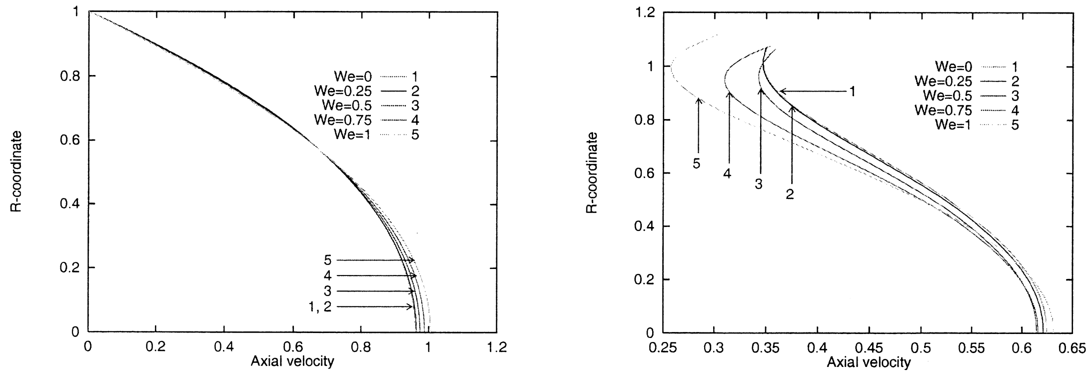

(g) V_z **profiles,** $0\leq We \leq 1$, **Z=-0.4** (h) V_z **profiles,** $0\leq We \leq 1$, **Z=0.4**

Figure 15 (*Continued*)

the centreline of the fluid for the STGFEM is given in Figure 19(b). The comparison with the Maxwell and Oldroyd-B fluid models clearly distinguishes the influence that viscoelasticity has, causing an increase in pressure drop. The normal stress invariant $trT - 3T_{\theta\theta}$ along the axis of symmetry in the die is given in Figure 19(c); the shift from and return to the zero level over the die exit region is apparent. With elasticity, there is a downstream shift of the minimum invariant values, a characteristic feature of exit flows. Again, there is close correspondence between Maxwell and Oldroyd-B profiles, confirming present solution accuracy.

Figure 20(a) shows the entry pressure loss as a function of Deborah number. The entry pressure loss is measured as the dimensionless Couette correction value C_{en}, defined as

$$C_{\text{en}} = \frac{(\delta_{\text{p}} - L_{\text{U}} \times \Delta p_{\text{U}} - L_{\text{D}} \times \Delta p_{\text{D}})}{(2\tau_{\text{w}})}$$

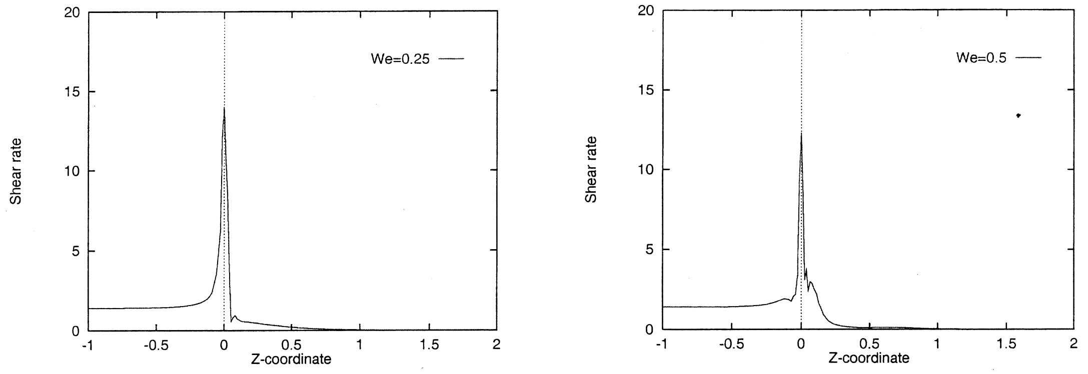

(a) We=**0.25**, I_2 **max=14.01**

(b) We=**0.5**, I_2 **max=12.29**

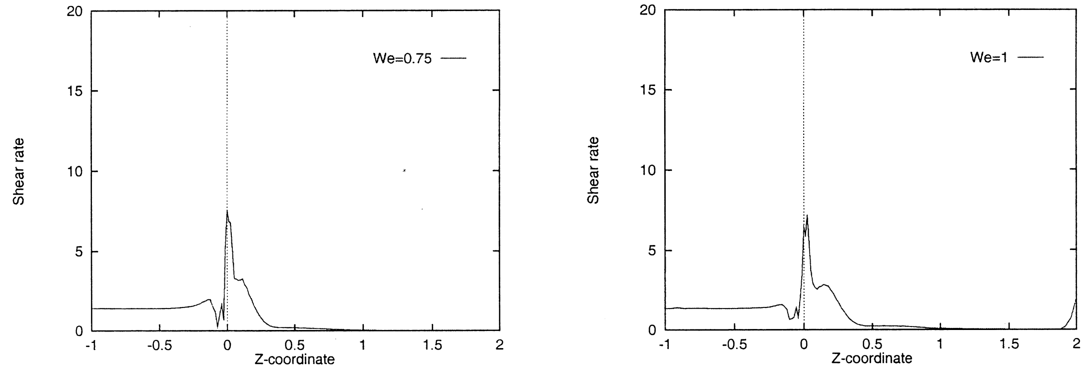

(c) We=**0.75**, I_2 **max=7.60**

(d) We=**1**, I_2 **max=7.19**

Figure 16. DSF: shear rate (I_2) on top surface, short mesh.

The terms L_{U} and L_{D} denote the upstream and downstream die lengths, while Δp_{U} and Δp_{D} are the associated pressure gradients for the fully developed upstream and downstream flows, respectively. The downstream wall shear stress in the die is represented by τ_{w}, and δ_{p} is the total pressure loss between the die entry and exit. The entry pressure loss for the three fluid models, namely PTT [42], Oldroyd-B (this work) and Maxwell fluids [5], are compared in Figure 20(a). For *De* values up to approximately 0.2, the Couette correction decreases in all cases. For higher values of *De* a monotonic increase in Couette correction occurs for the PTT model, as opposed to a steady decrease for the Oldroyd and Maxwell fluid. The different trends observed for PTT results on entry pressure loss may be attributed to the variations in extensional and viscous behaviour of this model. Experience from experimental studies would indicate that C_{en} increases with increasing *De*, generated via flow rate increase.

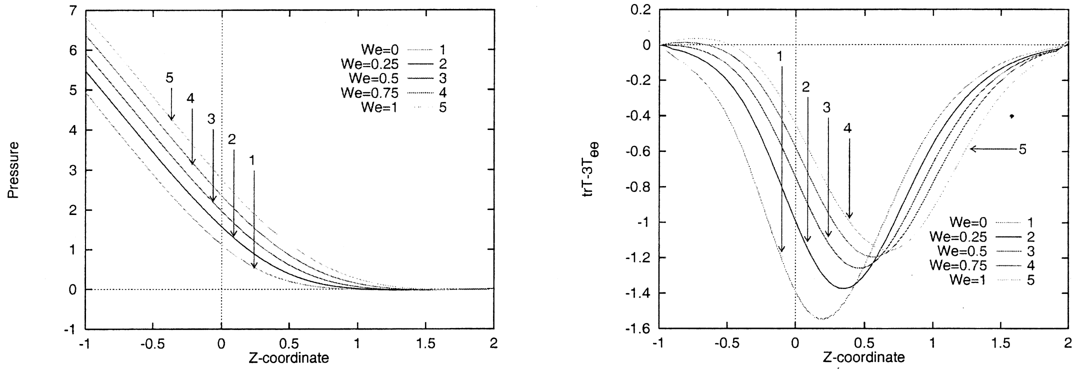

(a) **pressure** (b) $trT - 3T_{\theta\theta}$

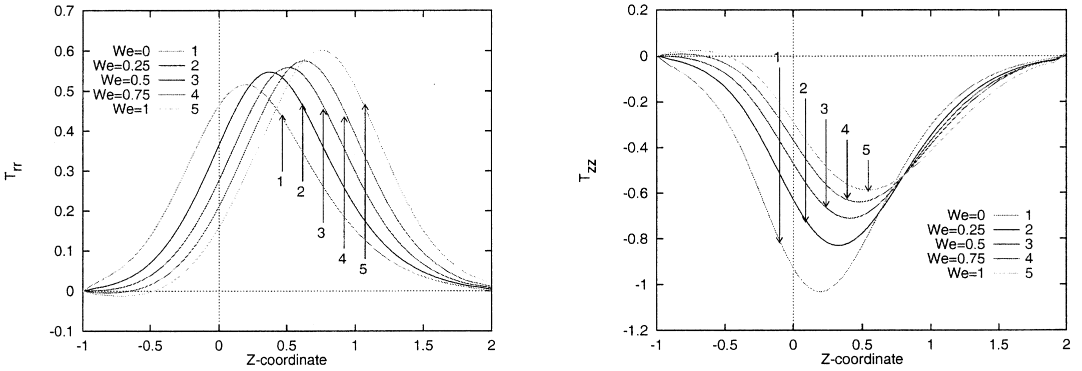

(c) **stress** T_{rr} (d) **stress** T_{zz}

Figure 17. DSF: line plot along the axis of symmetry, short mesh.

The exit pressure loss, an alternative quantifiable factor, is represented by the dimensionless Couette correction factor C_{ex}, defined as:

$$C_{\mathrm{ex}} = \frac{(\delta_{\mathrm{p}} - L_{\mathrm{U}} \times \Delta p_{\mathrm{U}})}{(2\tau_{\mathrm{w}})}$$

In Figure 20(b), exit pressure loss is compared for three fluid models over $0 \leq De \leq 1$; a Maxwell fluid [5] and two Oldroyd-B fluids [8] with partial viscosity ratios of $\mu_1/\mu_2 = 8$. Higher exit pressure losses occur for lower viscosity ratios. In this case, exit pressure loss consistently rises with increasing De.

Comparisons are made in Table IV between the theory of Tanner [4] and numerical solutions of Caswell and Viriyayuthakorn [5], Bush *et al.* [6], Crochet and Keunings [7] and the STGFEM solution of this paper. Table IV(a) covers results up to *De* of unity, whilst on longer geometries, Table IV(b) provides values for *De* beyond four.

Figure 21(a) demonstrates STGFEM die-swell profiles corresponding to the location for the free surface over the jet region, using an Oldroyd-B model. As anticipated, maximum swell corresponds to the instance with the largest Weissenberg number. Figure 21(b) catalogues the swelling ratio against the literature, including theoretical and numerical solutions for increasing Deborah number. The STGFEM results are observed to adhere closest to the results of Crochet and Keunings [8]. The theory of Tanner [4], is upheld for $De \leq 1.5$, beyond which

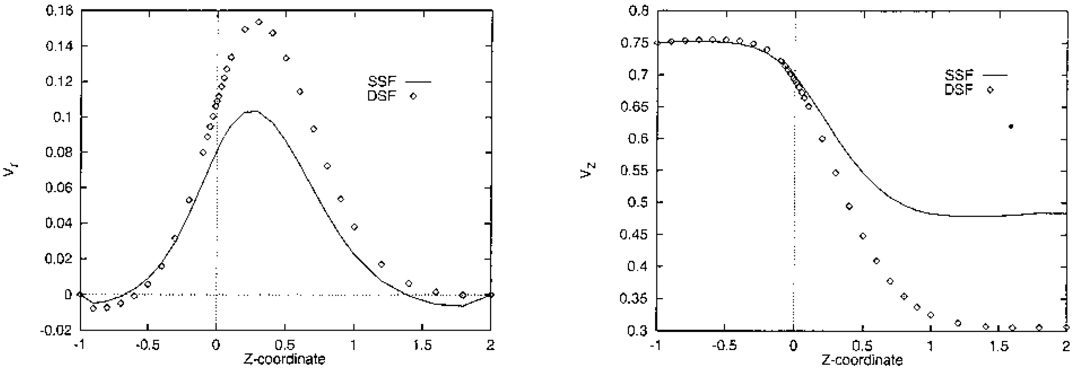

(a) velocity V_r

(b) velocity V_z

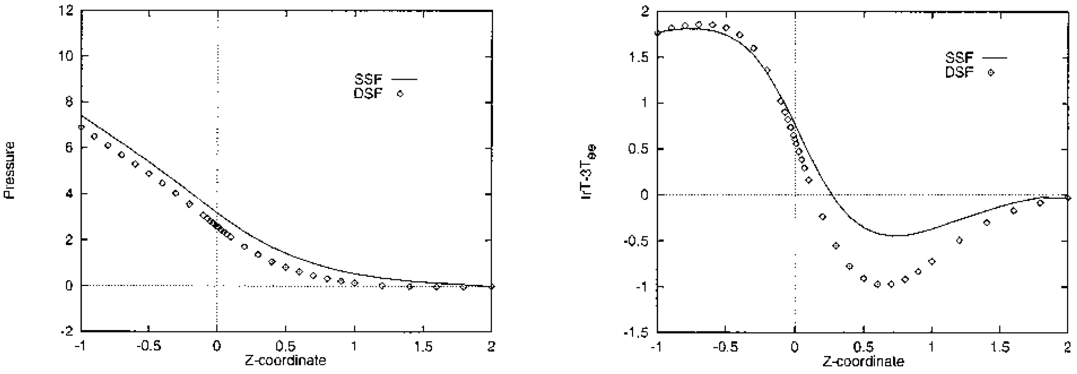

(c) pressure

(d) $trT - 3T_{\theta\theta}$

Figure 18. SSF and DSF: line plot along horizontal line $R = 0.5$, $We = 1$, short mesh.

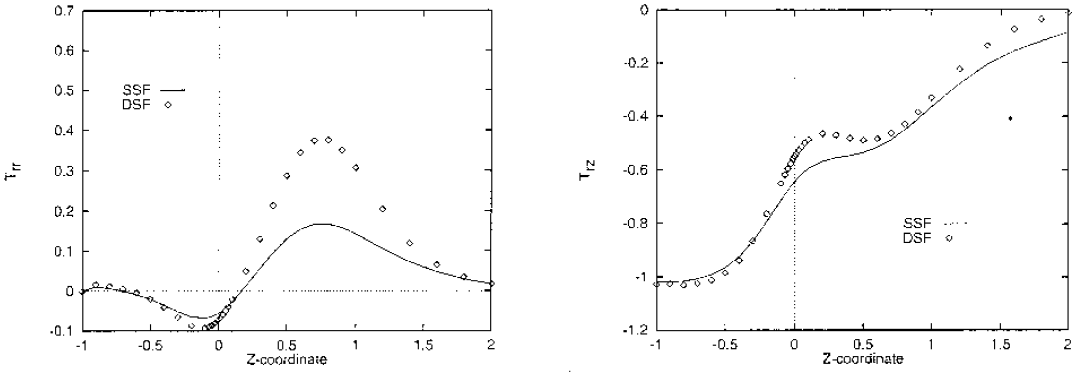

(e) stress T_{rr}

(f) stress T_{rz}

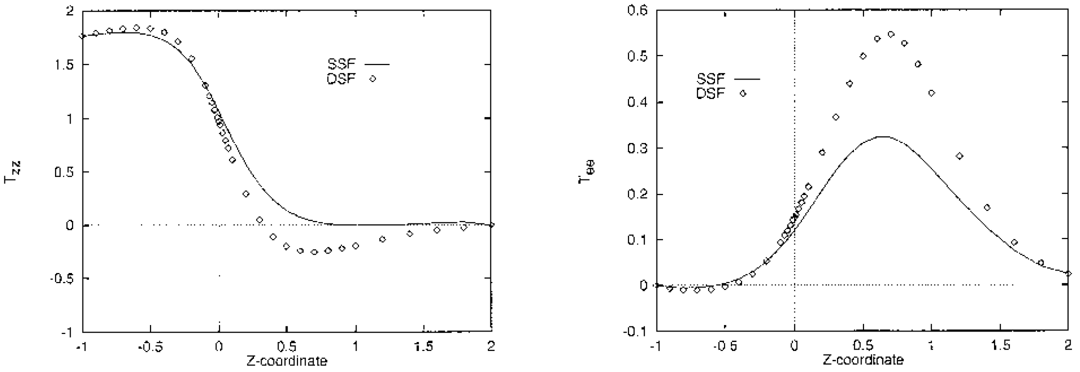

(g) stress T_{zz}

(h) stress $T_{\theta\theta}$

Figure 18 (*Continued*)

there is departure. This is taken as a strong indicating factor as to the high quality of the present solutions. It is noted, that with longer jet geometries, De^{lim} is increased to values approaching four. The key factor here is the jet length, once a die length has been specified that satisfies fully-developed inlet flow conditions. At die length:jet length of 0.5, De^{lim} is 2.0 for the short mesh and 3.0 for the medium mesh. For a ratio of 0.25, De^{lim} is increased to beyond 3.0 (to 3.2). See Figure 13 for the longer mesh pattern details and Figure 21 for swell.

6.4. *DSDF*

Extrema for pressure and stress in the case of DSDF are presented in Table V for a range of Weissenberg numbers from zero to a limiting value of 0.75.

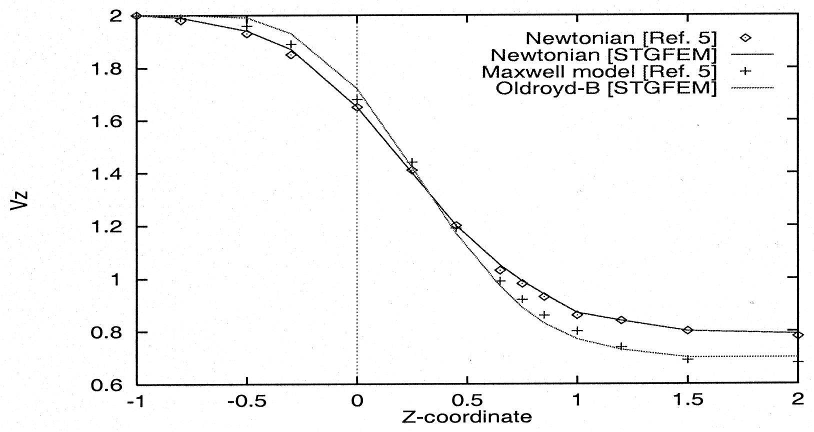

(a) **velocity** V_z

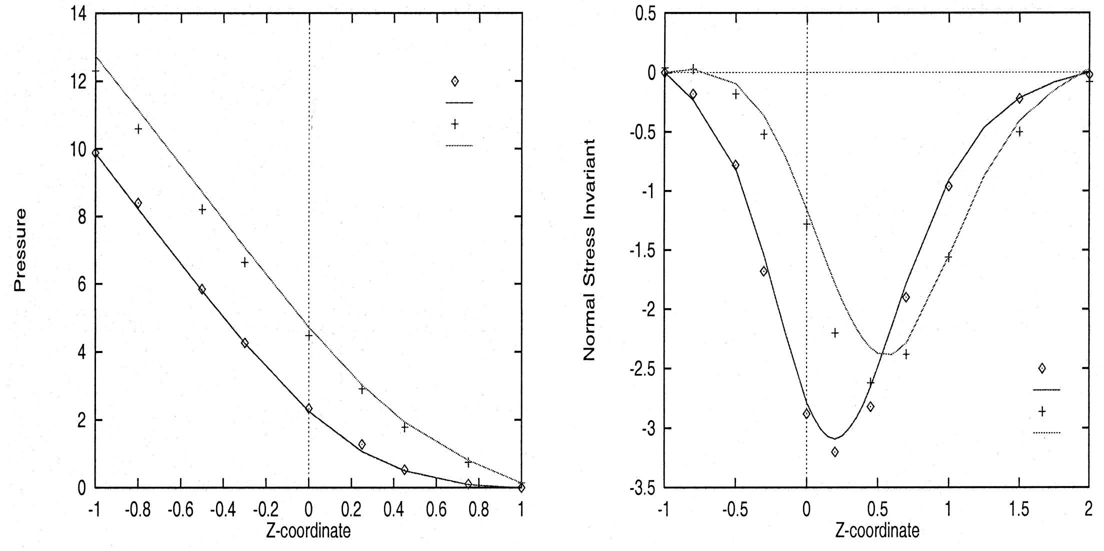

(b) **pressure**

(c) $trT - 3T_{\theta\theta}$

Figure 19. DSF: line plot along the axis of symmetry for Newtonian fluid, Maxwell fluid and Oldroyd-B fluid ($De = 1$), short mesh.

The top surface, I_2 profiles of Figure 22, reflect those of both DSF and SSDF combined. Peak values are still further elevated above those for DSDF (by 50 per cent), ranging from 16.5 for $We = 0.25$ to 9.48 for $We = 0.75$; representing a reduction of 42 per cent with We. Pre-die

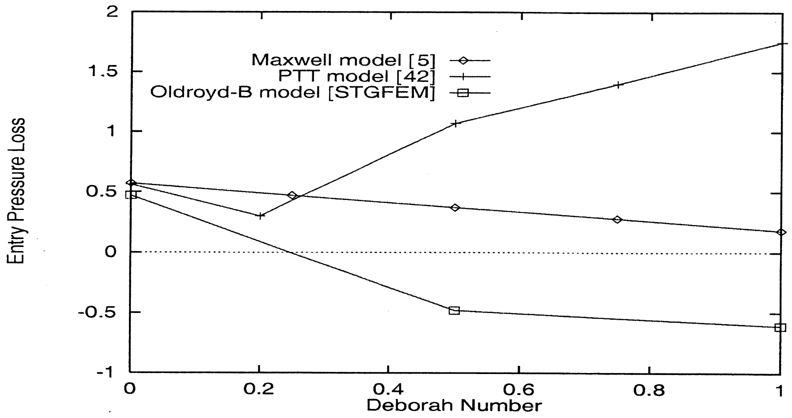

(a) **entry pressure loss**

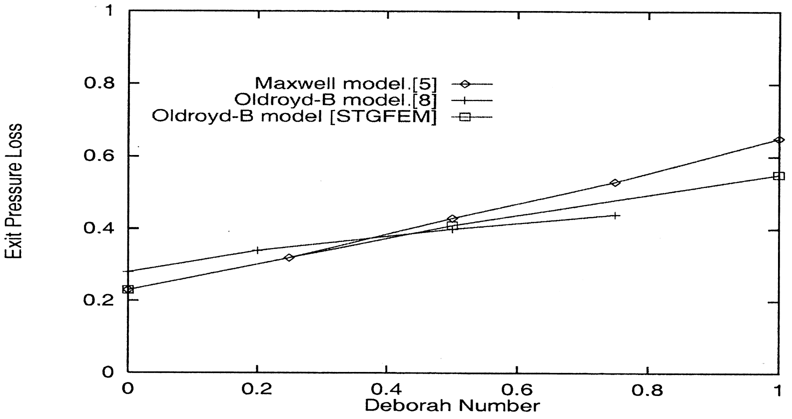

(b) **exit pressure loss**

Figure 20. DSF: pressure loss, short mesh.

exit undershoot is apparent beyond $We = 0.5$. Post-die exit recovery of I_2 follows similar trends to that observed for SSDF. As before, there is a minor increase of I_2 peak value from $We = 0.25$ to 0.5, prior to the subsequent decrease with increasing We.

SSDF and DSDF profile comparisons are made in Figure 23(a)–(h), as before mid-way over the top half of the die tube, $R = 0.5$, and for $We = 0.75$. Comparing radial velocities at the die exit reveals the typical profile shape, with the DSDF peak V_r value being 14 per cent higher than for SSDF, due to the influence of die exit swell (Figure 23(a)). The axial velocity variations over the die exit show an almost linear fall in V_z immediately after the die, followed by a gradual transition to a plug flow (Figure 23(b)). The swelling action to the extrudate results in a lower final fluid velocity, where that for DSDF is approximately 20 per cent less than for SSDF; this is due to the increased cross-sectional volume. Pressure profiles for both flow types are included in Figure 23(c). Pressure throughout the domain for DSDF is consistently lower than SSDF, although the general profile shape is almost identical. This

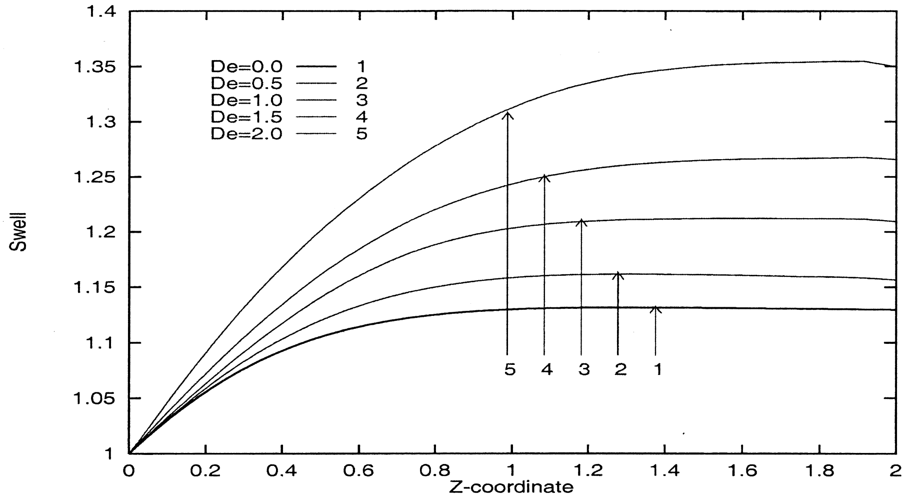

(a) **die swell on top surface, short mesh, $0 \leq De \leq 2$**

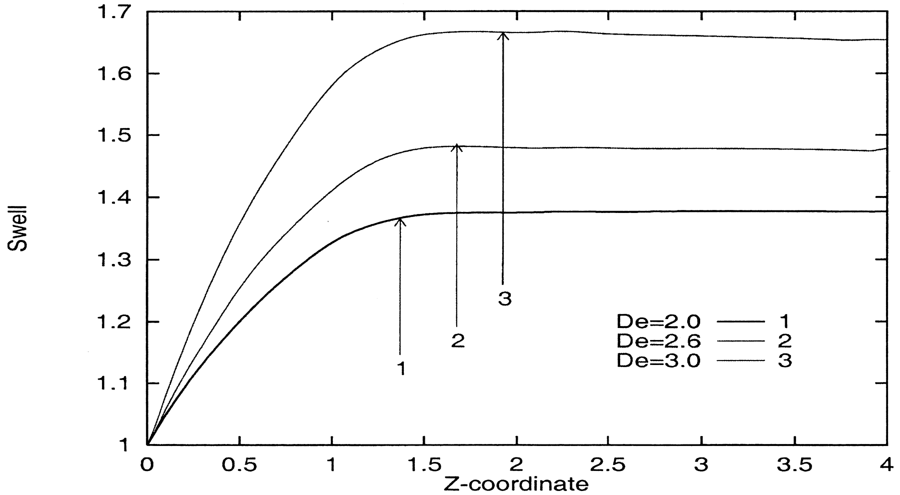

(b) **die swell on top surface, medium mesh, $2 \leq De \leq 3$**

Figure 21. DSF: die swell and swelling ratio.

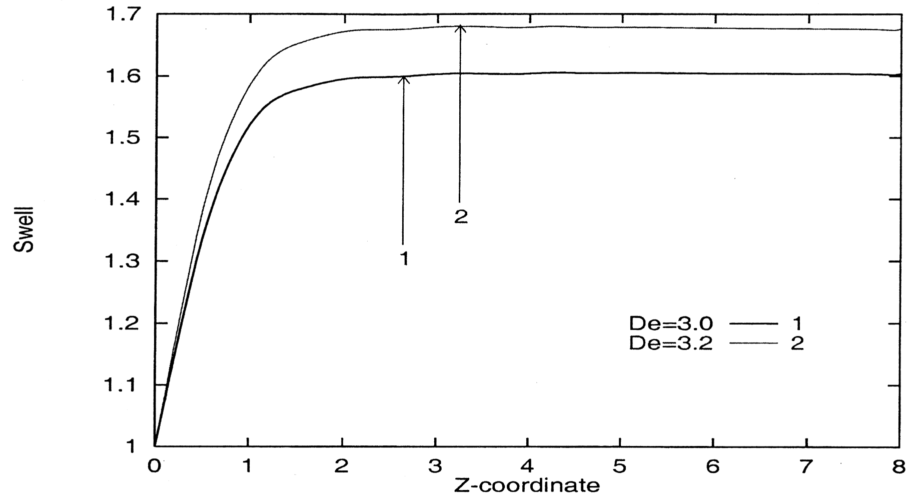

(c) **die swell on top surface, long mesh, $De \geq 3$**

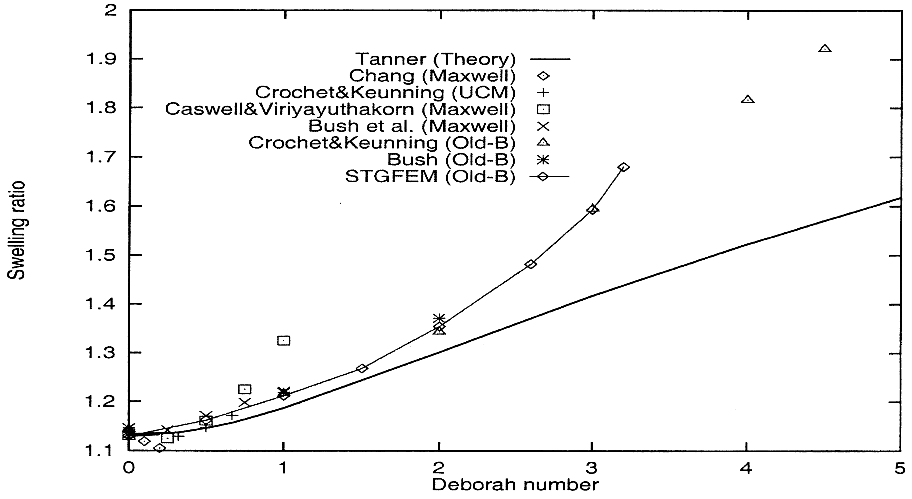

(d) **swelling ratio for theory and numerical solutions**

Figure 21 (*Continued*)

phenomenon may be attributed to the influence of die-swell. Figure 23(d) shows almost identical stress invariant profiles throughout the die exit region; the only exception is within the zone of maximum die-swell, where an increase in negative invariant of up to 25 per cent occurs for DSDF. The same effect is present in the dominant T_{zz} stress component of the

Table IV. (a) Swelling ratio for DSF, $0 \leq De \leq 1$; (b) swelling ratio for DSF, $1 \leq De \leq 4.5$.

Investigator	Model	*De*						
		0	0.25	0.33	0.5	0.67	0.75	1
(a)								
Tanner [4]	Theory	1.131	1.134	1.137	1.146	1.157	1.163	1.186
Caswell and Viriyayuthakorn [5]	Maxwell	1.131	1.125	–	1.161	–	1.225	1.325
Bush *et al.* [6]	Maxwell	1.134	1.142	–	1.171	–	1.198	1.221
Crochet and Keunings [7]	UC Maxwell	1.126	–	1.129	1.147	1.172	–	1.217
STGFEM	Oldroyd-B	1.130	–	–	1.162	–	–	1.212
		De						
		1	1.5	2	3	3.2	4	4.5
(b)								
Tanner [4]	Theory	1.187	1.242	1.301	1.417	1.440	1.523	1.572
Crochet and Keunings [8]	Oldroyd-B	1.217	–	1.343	1.595	–	1.817	1.921
Bush [35]	Oldroyd-B	1.219	–	1.371	–	–		–
Clermont and Normandin [36]	Oldroyd-B	1.210	–	1.380	1.470	–	1.530	–
STGFEM	Oldroyd-B	1.212	1.268	1.354	1.593	1.680	–	–

invariant in Figure 23(g). The radial extra-stress component profiles of Figure 23(e) follow the anticipated trends, with the die-swell influence of the DSDF, resulting in a major stress increase of 30 per cent at $z = 0.55$. The shear stress of Figure 23(f) illustrates the gradual decline in T_{rz} as the fluid exits the die. The DSDF shear stress outside the die tends to sustain a presence, larger in contrast to that for SSDF, due to the decreased internal stressing that

Table V. DSDF: pressure and stress for various *We*.

	Solutions	$We = 0$	$We = 0.25$	$We = 0.5$	$We = 0.75$
P	min	−8.40	−2.69	−1.35	−0.75
	max	6.79	8.78	21.3	42.1
τ_{rr}	min	−5.56	−2.51	−3.05	−1.88
	max	0.58	0.84	6.18	20.7
τ_{rz}	min	−10.4	−5.12	−8.37	−517
	max	3.00	4.50	12.4	12.8
τ_{zz}	min	−0.89	−3.44	−9.47	−11.06
	max	16.7	23.1	25.2	29.7
$\tau_{\theta\theta}$	min	−0.01	−0.02	−0.01	−0.01
	max	0.38	0.39	0.34	0.34

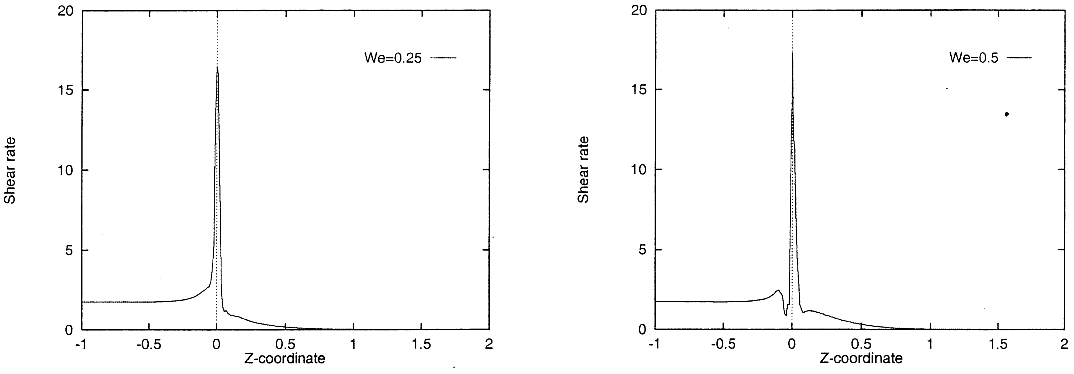

(a) We**=0.25,** I_2 **max=16.45** (b) We**=0.5,** I_2 **max=17.33**

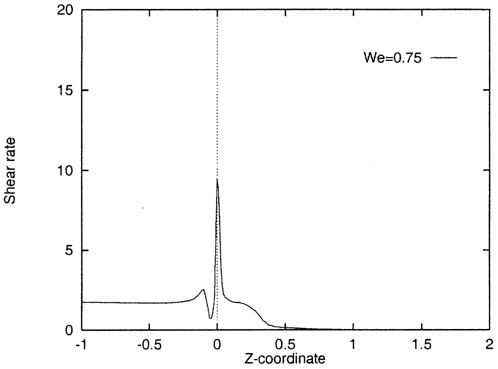

(c) We**=0.75,** I_2 **max=9.48**

Figure 22. DSDF: shear rate (I_2) on top surface.

results from the swelling. Understandably, the $T_{\theta\theta}$ stress profile of Figure 23(h) for DSDF is 25 per cent higher than that for SSDF, again due to the extrudate swelling.

Similarities and differences between DSF and DSDF at the die exit and jet region are investigated in Figure 24 with $We = 0.75$, for the upper half of the die along the horizontal line $R = 0.5$. This comparison highlights the influence of the additional drag flow component upon extrusion flow, where the free surface finds its own location. The parabolic radial velocity profiles of Figure 24(a) show peak values in the area, just downstream of the die exit. DSDF reaches a peak of 19 per cent lower than that of DSF, due to the suppressive effects on V_r by the axially moving boundary (travelling wire), which is also responsible for maintaining the upstream axial velocity of DSDF at a level approximately 5 per cent higher than for DSF (Figure 24(b)). The increased axial upstream velocity of DSDF also results in a higher internal pressure before the die exit (Figure 24(c)). The stress invariant profiles of Figure 24(d) display upstream DSF invariant maxima of 1.3, 60 per cent higher than that of DSDF. This is a result of the dragging effect of the moving boundary aiding the fluids movement inside the die, therefore reducing axial extra-stress, the dominant stress component of the invariant (Figure 24(g)). The drag imposed by the moving boundary has an opposite effect on the radial extra-stress profiles of Figure 24(e), with DSDF stresses 32 per cent higher than those for DSF, because of the larger swell of the extrudate. For both flow types, a non-monotonic climb to vanishing shear stress is observed as the fluid exits the die (Figure 24(f)); as above, the drag flow instance sustains a larger shear stress. As expected, the $T_{\theta\theta}$ stress profiles of Figure 24(h) give a smaller maxima than in DSDF, approximately 38 per cent less than for DSF.

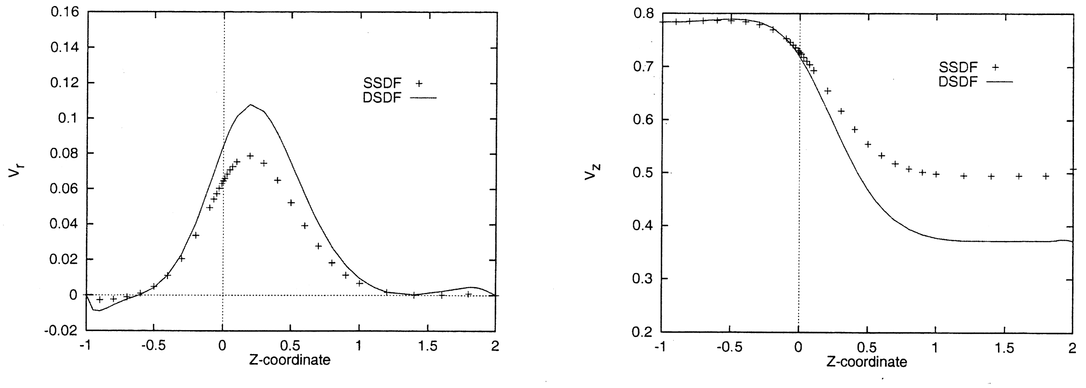

(a) **velocity** V_r

(b) **velocity** V_z

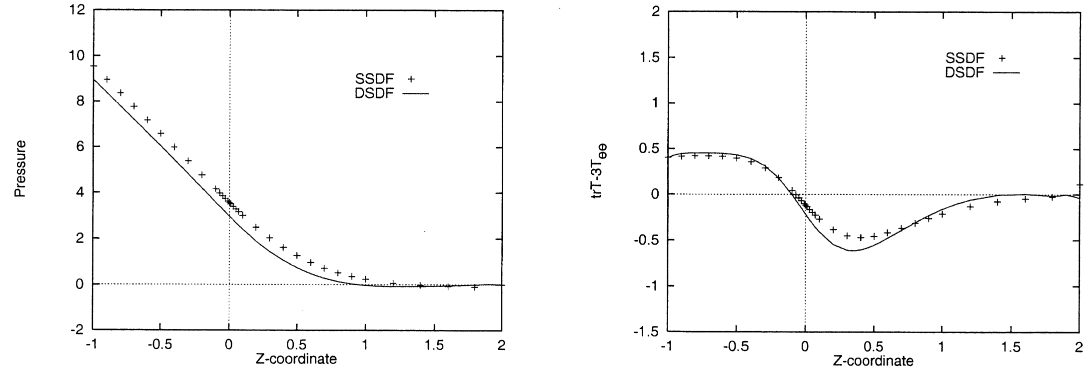

(c) **pressure**

(d) $trT - 3T_{\theta\theta}$

Figure 23. SDSF and DSDF: line plot along horizontal line $R = 0.5$, $We = 0.75$.

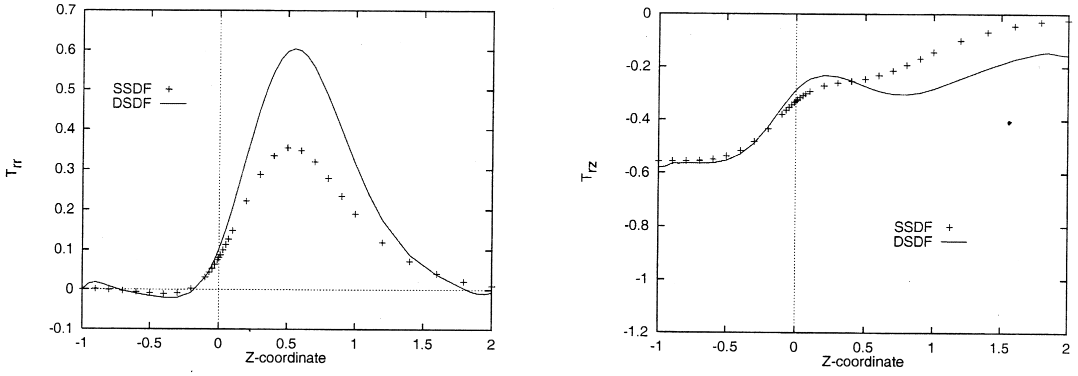

(e) stress T_{rr}

(f) stress T_{rz}

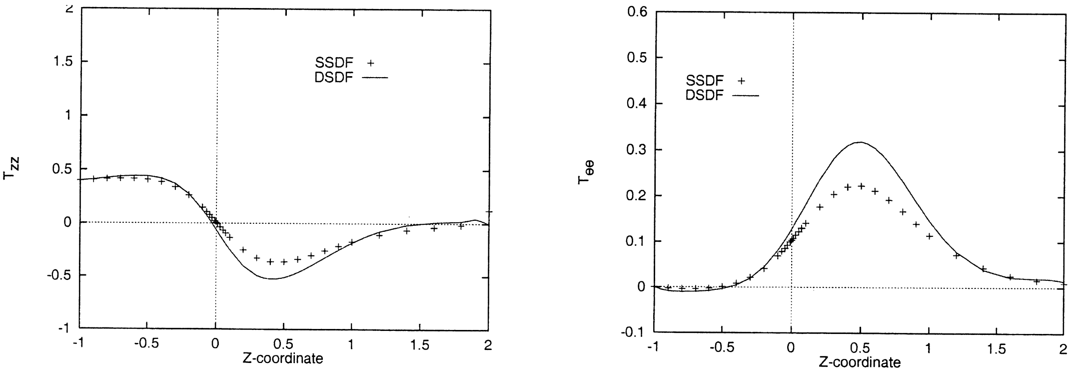

(g) stress T_{zz}

(h) stress $T_{\theta\theta}$

Figure 23 (*Continued*)

7. CONCLUSIONS

This study has provided an analysis of steady free surface flows for an Oldroyd-B fluid using a Taylor–Galerkin/pressure-correction method with consistent streamline upwinding and velocity gradient recovery. Various cases studied have contrasted stick-slip to die-swell flows. In addition, a superimposed drag flow component to each class of flow has facilitated further comparison. Our solutions for SSF agree to within O(1 per cent) with the theoretical solution of Trogdon and Joseph [3] for Newtonian flow. Swelling ratios in DSF compare favourably against both theory and numerical solutions for increasing *We*. Present results are observed to adhere to the theory of Tanner [4] up to *De* of 1.5. The limiting value of *We* for converged solutions in stick-slip instances is 1.7 for short geometries, 2.0 on medium geometries and 2.2 for long geometries. Equivalently, converged solutions for DSF are observed for Weissenberg numbers ranging from zero to a limit of unity on short geometries, increasing to 1.6 on longer geometries. This compares favourably with the literature. It is noted that, longer jet lengths are crucial to achieve higher limiting elasticity number solutions.

In the comparisons for stick-slip flow, with and without drag flow, the effect of the additional drag component gives rise to larger values of V_z, pressure, T_{rr}, and T_{rz} than would otherwise be the case. In contrast V_r, T_{zz} and $T_{\theta\theta}$ are reduced. This response also holds for die-swell and DSDF cases. For SSDF, the upstream linear pressure profile decreases uniformly tending towards the die exit, where a highly concentrated build up is observed at the singularity, reaching a peak value 40 per cent higher than for pure SSF. The maximum $T_{\theta\theta}$ stress component has shifted upward away from the lower free boundary into the core flow. Axial stress T_{zz} at the lower boundary is much higher than for the SSF. T_{zz} for SSDF is less than half that of SSF, so that drag flow and increasing elasticity reduces axial stress interior to the domain.

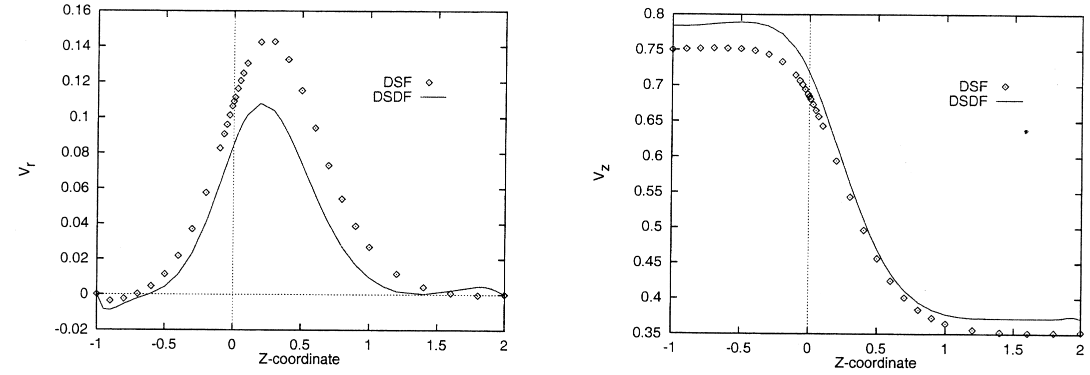

(a) **velocity** V_r

(b) **velocity** V_z

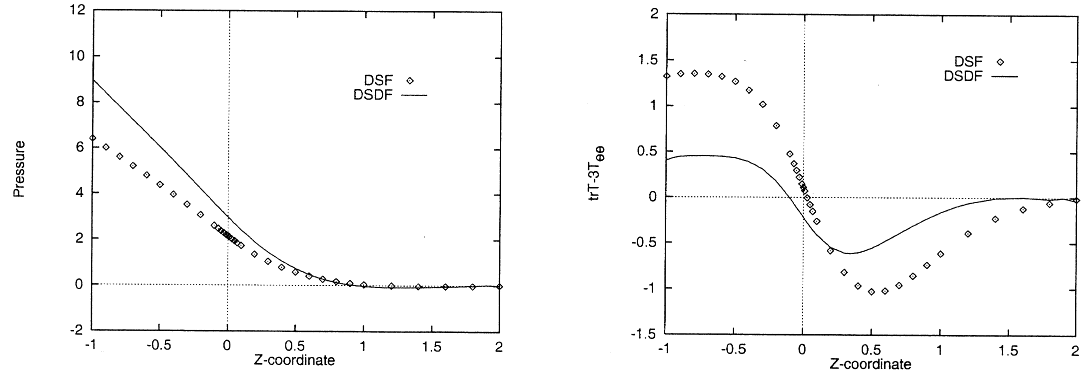

(c) **pressure**

(d) $trT - 3T_{\theta\theta}$

Figure 24. DSF and DSDF: line plot along horizontal line $R = 0.5$, $We = 0.75$.

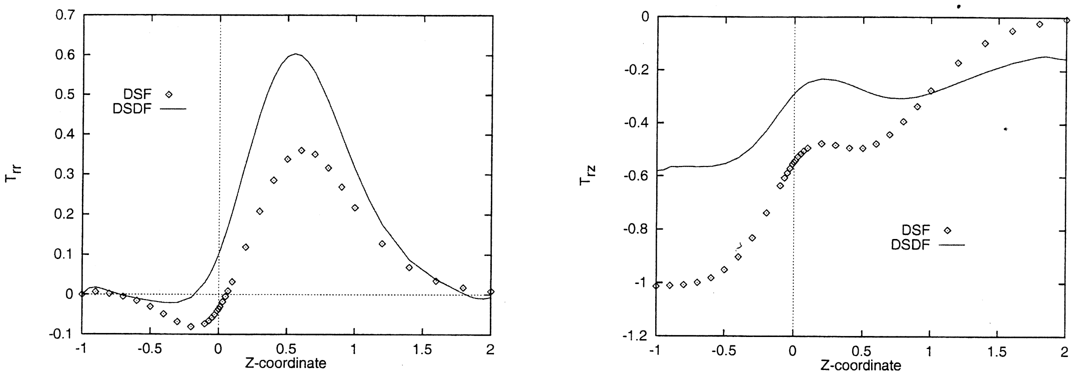

(e) stress $\mathbf{T}_{rr}$ (f) stress $\mathbf{T}_{rz}$

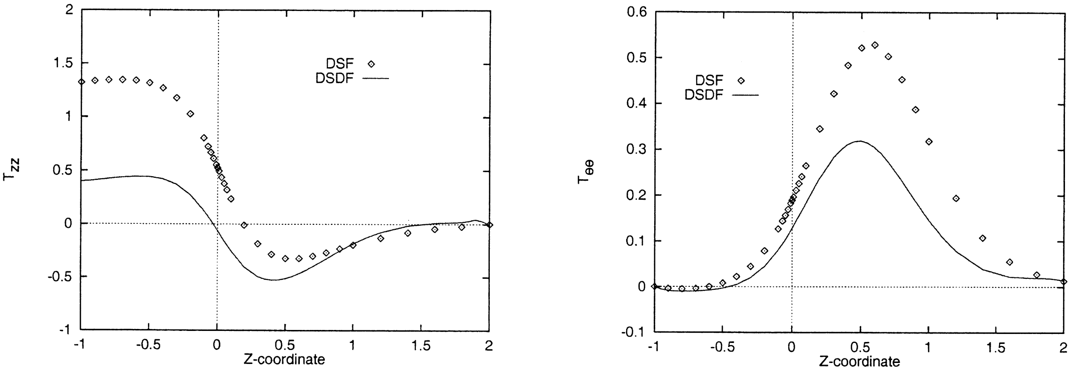

(g) stress $\mathbf{T}_{zz}$ (h) stress $\mathbf{T}_{\theta\theta}$

Figure 24 (*Continued*)

For DSF, comparison of Newtonian results against those for Maxwell and Oldroyd models clearly distinguishes the influence that viscoelasticity has, causing an increase in pressure drop. With elasticity, there is a downstream shift in minimum stress invariant a characteristic feature of extrudate flows. Correspondence between Maxwell and Oldroyd profiles provides close agreement, confirming present solution accuracy. For *We* values up to approximately 0.2, the Couette correction *entry pressure* loss decreases in all cases. Observations confirm that for higher values of *We*, a monotonic increase in this Couette correction factor occurs for a PTT model, as opposed to a steady decrease for the Oldroyd and Maxwell fluids. Higher *exit pressure* losses occur for lower viscosity ratios and this factor consistently rises with increasing *We*.

We point to the particularly effective new free-surface location procedure adopted, herein, the pressure-drop/mass balance scheme. This, in conjunction with longer geometries, has provided more stable and accurate swelling predictions, at higher levels of elasticity than would otherwise have been the case.

At the singularity zone for DSF, a localized pressure pocket emerges which is two and a half times larger than for SSF cases; T_{rr} trebles and T_{rz} doubles over SSF. The extrudate in DSF gives rise to larger values of V_r, T_{rr}, T_{rz} and $T_{\theta\theta}$ in contrast to SSF. In addition beyond the die, the extrudate is responsible for a decrease in V_z, pressure, and T_{zz}. This is again true when drag flow is incorporated within this die-swell setting.

The trends in top surface I_2 profiles rather symbolize the differences observed between the four flows studied. Peak I_2 values on top surfaces correspond to die-exit location. Superimposed drag flow induces increase in I_2 maxima and sustains post-die exit recovery. DSF also elevates I_2 maxima above stick-slip alternatives. Pre-die exit undershoots are noted in all flows at the larger values of *We*, occurring earlier in *We* for DSF over stick-slip counterparts, and are slightly more prominent in drag flow instances. Post-die exit local minima in I_2 arise for DSF at the larger end of the *We* value range; these become elongated and flatten out with the additional drag flow component. Oscillations in I_2 profiles, particularly pre-die exit, could be taken as indicators of imminent onset of instability.

APPENDIX A

To derive an annular inlet Newtonian drag flow profile, we follow Bird [44] and use a non-dimensional equation for annular pressure-driven flow,

$$V_z(r) = \frac{Pb^2}{4\mu L}\left\{1 - \left(\frac{r}{b}\right)^2 + \frac{1}{\ln(a/b)}\left[\left(\frac{a}{b}\right)^2 - 1 + \frac{4\mu L V_{\text{wire}}}{Pb^2}\right]\ln\left(\frac{r}{b}\right)\right\} \tag{A.1}$$

with variables of viscosity μ, length Z_1Z_2 (Figure 2(b) or (d)) L, pressure drop between inlet and outlet P, wire speed V_{wire}, inner annular radius a and outer radius b.

Subsequently, we may derive the flowrate at inlet and relate this to pressure drop, via

$$Q = 2\pi \int_a^b r V_z(r)\,\mathrm{d}r \tag{A.2}$$

Hence, once flow rate Q is prescribed (say from an outlet plug or free jet flow), we may evaluate the pressure drop from the constant term, $Pb^2/4\mu L$, utilizing Equation (A.1) for $V_z(r)$ within Equation (A.2).

In our present study for comparison purposes, we have recourse to the Newtonian streamfunction solution for axisymmetric SSF, as developed in the article of Trogdon and Joseph [3]

Case $z > 0$:

$$\begin{aligned}\psi(r,z) &= \frac{r^2}{4} - \sum_{m=1}^{\infty} \frac{1}{q_m^2 B_-(-iq_m)} \frac{rzJ_1(rq_m)}{J_0(q_m)} \mathrm{e}^{-zq_m} + \sum_{m=1}^{\infty} \operatorname*{Lim}_{\omega\to -iq_m} \frac{\mathrm{d}}{\mathrm{d}\omega}\left[\frac{i}{\omega^2 B_-(\omega)}\right] \frac{rJ_1(rq_m)}{J_0(q_m)} \mathrm{e}^{-zq_m}\end{aligned}$$

Case $z < 0$:

$$\psi(r, z) = r^2\left(\frac{1}{2} - \frac{r^2}{4}\right) + 2\mathscr{R}\left\{\sum_{m=1}^{\infty} \frac{B_+(ip_m)e^{zp_m}}{p_m J_1^2(p_m)} [rJ_0(p_m)J_1(rp_m) - r^2 J_1(p_m)J_0(rp_m)]\right\}$$

where

$$B_+(\omega) = -\frac{1}{4}\prod_{n=1}^{\infty} \frac{(1 + (\omega/\omega_n))(1 - (\omega/\bar{\omega}_n))}{(1 + (\omega/iq_n))^2}$$

and

$$B_-(\omega) = \prod_{n=1}^{\infty} \frac{(1 - (\omega/\omega_n))(1 + (\omega/\bar{\omega}_n))}{(1 - (\omega/iq_n))^2}$$

$J_k(x)$ is defined to be a Bessel function of the first kind, of integral order k expressed in series form as

$$J_k(x) = \sum_{n=0}^{\infty} \frac{(-1)^n}{n!(k+n)!}\left(\frac{x}{2}\right)^{k+2n}$$

where

$$q_n \approx \frac{\pi}{4}(4n+1) - \frac{3}{2\pi(4n+1)}, \qquad p_n = Z_n + \delta_n, \quad n = 1, 2, 3, \ldots$$

$$Z_n = \frac{1}{2}(\xi_n - \eta_n) + \frac{1}{4}i(2\ln 2\xi_n + \eta_n^2), \quad \xi_n = (2n+1)\pi$$

$$\eta_n = \frac{\ln 2\xi_n}{\xi_n}, \qquad \delta_n = -\frac{F'(Z_n)}{F(Z_n)}, \qquad F(x) = xJ_0^2(x) - 2J_0(x)J_1(x) + xJ_1^2(x)$$

$\bar{\omega}_n$ is complex conjugate of ω_n and $\bar{\omega}_n = -\hat{i}p_n$.

REFERENCES

1. Ngamaramvaranggul V, Webster MF. Computation of free surface flows with a Taylor–Galerkin/pressure-correction algorithm. *International Journal for Numerical Methods in Fluids* 2000a; **33**: 993–1026.
2. Ngamaramvaranggul V, Webster MF. Simulation of coating flows with slip effects. *International Journal for Numerical Methods in Fluids* 2000b; **33**: 961–992.
3. Trogdon SA, Joseph DD. The stick-slip problem for a round jet. II. Small surface tension. *Rheology Acta* 1981; **20**: 1–13.
4. Tanner RI. A theory of die-swell. *Journal of Polymer Science Part A* 1970; **8**: 2067–2078.
5. Caswell B, Viriyayuthakorn M. Finite element simulation of die swell for a Maxwell fluid. *Journal of Non-Newtonian Fluid Mechanics* 1983; **12**: 13–29.
6. Bush MB, Milthorpe JF, Tanner RI. Finite element and boundary element methods for extrusion computations. *Journal of Non-Newtonian Fluid Mechanics* 1984; **16**: 37–51.

7. Crochet MJ, Keunings R. Die swell of a Maxwell fluid numerical prediction. *Journal of Non-Newtonian Fluid Mechanics* 1980; **7**: 199–212.
8. Crochet MJ, Keunings R. Finite element analysis of die swell of a highly elastic fluid. *Journal of Non-Newtonian Fluid Mechanics* 1982; **10**: 339–356.
9. Matallah H, Townsend P, Webster MF. Recovery and stress-splitting schemes for viscoelastic flows. *Journal of Non-Newtonian Fluid Mechanics* 1998; **75**: 139–166.
10. Matallah H, Townsend P, Webster MF. Viscoelastic multi-mode simulation of wire-coating'. *Journal of Non-Newtonian Fluid Mechanics* 2000; **90**: 217–241.
11. Carew EOA, Townsend P, Webster MF. A Taylor-Petrov–Galerkin algorithm for viscoelastic flow. *Journal of Non-Newtonian Fluid Mechanics* 1993; **50**: 253–287.
12. Brooks AN, Hughes TJR. Streamline upwind/Petrov–Galerkin formulations for convection dominated flows with particular emphasis on the incompressible Navier–Stokes equation. *Computer Methods in Applied Mechanics & Engineering* 1982; **32**: 199–259.
13. Shakib F. PhD dissertation, Stanford University, 1987.
14. Hawken DM, Tamaddon-Jahromi HR, Townsend P, Webster MF. A Taylor–Galerkin-based algorithm for viscous incompressible flow. *International Journal for Numerical Methods in Fluids* 1990; **10**: 327–351.
15. Szady MJ, Salomon TR, Liu AW, Bornside DE, Armstrong RC, Brown RA. A new mixed finite element method for viscoelastic flows governed by differential constitutive equations. *Journal of Non-Newtonian Fluid Mechanics* 1995; **59**: 215–243.
16. Matallah H. Numerical simulation of viscoelastic flows. PhD thesis, University of Wales, Swansea, 1998.
17. Baloch A, Townsend P, Webster MF. On two and three dimensional expansion flows. *Journal of Computational Fluids* 1995; **24**(8): 863–882.
18. Baloch A, Townsend P, Webster MF. On vortex development in viscoelastic expansion and contraction flows. *Journal of Non-Newtonian Fluid Mechanics* 1996; **65**: 133–149; On two and three dimensional expansion flows. *Journal of Computational Fluids* 1995; **24**(8): 863–882.
19. Hassager O, Henriksen P, Townsend P, Webster MF, Ding D. The quarterbend: a three-dimensional benchmark problem. *Journal of Computational Fluids* 1991; **20**(4): 373–386.
20. Ding D, Townsend P, Webster MF. On computation of two and three-dimensional unsteady thermal non-Newtonian flows. *International Journal for Numerical Methods in Heat Fluid Flow* 1995; **5**(6): 495–510.
21. Tamaddon-Jahromi HR, Townsend P, Webster MF. Flow past a cylinder with and without an appurtenance. *International Journal for Numerical Methods in Engineering* 1993; **36**: 3991–4008.
22. Tamaddon-Jahromi HR, Townsend P, Webster MF. Unsteady viscous flow past a flat plate orthogonal to the flow. *Journal of Computational Fluids* 1994; **23**(2): 433–469.
23. Mutlu I, Townsend P, Webster MF. Computation of viscoelastic cable coating flows. *International Journal for Numerical Methods in Fluids* 1998; **26**: 697–712.
24. Mutlu I, Townsend P, Webster MF. Simulation of cable-coating viscoelastic flows with coupled and decoupled schemes. *Journal of Non-Newtonian Fluid Mechanics* 1998; **74**: 1–23.
25. Matallah H, Townsend P, Webster MF. Viscoelastic computations of polymeric wire-coating flows. *International Journal for Numerical Methods in Engineering* 2001 (in press).
26. Wapperom P, Webster MF. A second-order hybrid finite element/volume method for viscoelastic flow. *Journal of Non-Newtonian Fluid Mechanics* 1998; **79**: 405–431.
27. Wapperom P, Webster MF. Simulation for viscoelastic flow by a finite volume/element method. *Applied Mechanical Engineering* 1999; **180**: 281–304.
28. Marchal JM, Crochet MJ. A new mixed finite element for calculating viscoelastic flow. *Journal of Non-Newtonian Fluid Mechanics* 1987; **26**: 77–114.
29. Coleman CJ. On the use of boundary integral methods in the analysis of non-Newtonian fluid flow. *Journal of Non-Newtonian Fluid Mechanics* 1984; **16**: 347–355.
30. Owens RG, Phillips TN. A spectral domain decomposition method for the planar non-Newtonian stick-slip problem. *Journal of Non-Newtonian Fluid Mechanics* 1991; **41**: 43–79.
31. Rosenberg J, Keunings R. Numerical integration of differential viscoelastic models. *Journal of Non-Newtonian Fluid Mechanics* 1991; **39**: 269–290.
32. Baaijens FPT. Numerical experiments with a discontinuous Galerkin method including monotonicity enforcement on the stick-slip problem. *Journal of Non-Newtonian Fluid Mechanics* 1994; **51**: 141–159.
33. Nickell RE, Tanner RI, Caswell B. The solution of viscous incompressible jet and free-surface flows using finite-element methods. *Journal of Fluid Mechanics Part 1* 1974; **65**: 189–206.
34. Chang PW, Patten TW, Finlayson BA. Collocation and Galerkin finite element methods for viscoelastic fluid flow—II. Die-swell problems with a free surface. *Computers and Fluids* 1979; **7**: 285–293.
35. Bush MB. A numerical study of extrudate swell in very dilute polymer solutions represented by the Oldroyd-B model. *Journal of Non-Newtonian Fluid Mechanics* 1990; **34**: 15–24.

36. Clermont JR, Normandin M. Numerical simulation of extrudate swell for Oldroyd-B fluid using the stream-tube analysis and a streamline approximation. *Journal of Non-Newtonian Fluid Mechanics* 1993; **50**: 193–215.
37. Oldroyd JG. On the formulation of rheological equations of state. *Proceedings of the Royal Society* 1950; **A200**: 523–541.
38. Holstein H. PhD thesis, University of Wales, Aberystwyth, 1981.
39. Townsend P, Webster MF. An algorithm for the three-dimensional transient simulation of non-Newtonian fluid flows. In *Proceedings of the International Conference NUMETA 1987*, Swansea, Pande GN, Middleton J (eds). Nijhoff: Dordrecht, 1987.
40. Levine N. Superconvergent recovery of the gradients from linear finite element approximation on triangle. Technical Report Numerical Analysis Report 6/83, University of Reading, 1983.
41. Levine N. Superconvergent estimation of the gradients from finite element approximation of triangle elements. PhD thesis, University of Reading, 1985.
42. Crochet MJ, Davies AR, Walters K. *Numerical Simulation of Non-Newtonian Flow*, *Rheology Series 1*. Elsevier Science Publishers: Amsterdam, 1984.
43. Silliman WJ, Scriven LE. Separating flow near a static contact line: slip at a wall and shape of a free surface. *Journal of Computational Physics* 1980; **34**: 287–313.
44. Bird RB, Steward WE, Lightfoot EN. *Transport Phenomena*. Wiley: New York, 1960.